

Optimal On-board Abort Guidance based on Successive Convexification for Atmospheric Re-Entry

Dominguez Calabuig, G.J.; Mooij, E.

DOI

[10.2514/6.2021-0860](https://doi.org/10.2514/6.2021-0860)

Publication date

2021

Document Version

Final published version

Published in

AIAA Scitech 2021 Forum

Citation (APA)

Dominguez Calabuig, G. J., & Mooij, E. (2021). Optimal On-board Abort Guidance based on Successive Convexification for Atmospheric Re-Entry. In *AIAA Scitech 2021 Forum: 11–15 & 19–21 January 2021, Virtual Event* Article AIAA 2021-0860 American Institute of Aeronautics and Astronautics Inc. (AIAA). <https://doi.org/10.2514/6.2021-0860>

Important note

To cite this publication, please use the final published version (if applicable). Please check the document version above.

Copyright

Other than for strictly personal use, it is not permitted to download, forward or distribute the text or part of it, without the consent of the author(s) and/or copyright holder(s), unless the work is under an open content license such as Creative Commons.

Takedown policy

Please contact us and provide details if you believe this document breaches copyrights. We will remove access to the work immediately and investigate your claim.



Optimal On-board Abort Guidance based on Successive Convexification for Atmospheric Re-Entry

G.J. Dominguez Calabuig* and E. Mooij†

*Delft University of Technology, Faculty of Aerospace Engineering,
Kluyverweg 1, 2629 HS Delft, The Netherlands*

Space safety and hazard-reduction techniques for space-transportation vehicles are becoming critical in the advent of commercial crewed launches and suborbital intercontinental travel. One way to mitigate risks is to use advanced guidance strategies to centralise mission planning, and guidance, navigation and control. Convex optimisation can be suitable for this purpose, as it solves second-order-cone programming problems sequentially in polynomial time. As atmospheric re-entry contains a large number of non-convexities, an advanced optimal-control optimiser based on successive convex optimisation was developed and analysed with a golden-section line-search method to enhance its convergence. A direct-linearisation approach, although slightly sensitive to initial guesses, was seen to be robust when compared in different objective formulations. However, a hybrid approach using a lossless convexification performed better for most problems, although it relied on a regularisation condition, which was sometimes difficult to satisfy. The reachability capabilities of the SPHYNX lifting body during orbital and descent aborts were analysed and showed that around 14 minutes are available to perform an abort to an alternative landing site for a nominal mission. While there is significant room for improvement, the study shows that successive convex optimisation could be potentially used for mission planning and on-board applications as an optimal trajectory planner during realistic re-entry missions.

Nomenclature

c^*	Chapman equation constant = $1.1097 \times 10^8 \text{ Wm}^{-1/2}$
C_L	Lift aerodynamic coefficient, -
C_D	Drag coefficient, -
D	Drag force, N
f	Earth flattening factor = $1/298.257223563$, -
g	Gravitational acceleration, m/s^2
g_R	Gravitational acceleration in radial direction, m/s^2
g_δ	Gravitational acceleration in meridional direction, m/s^2
h	Altitude (or Geodetic Altitude), m
J	Scaled Non-linear Objective Function, -
J_a	Scaled Augmented Non-linear Objective Function, -
\tilde{J}_a	Scaled Augmented Non-linear Objective Function used for the adaptive thrust region, -
J_2	Zonal harmonic coefficient of degree 2 = 1.082627×10^{-3} , -
L	Lift force, N
L	Scaled Linearised Objective Function, -
L_a	Scaled Augmented Linearised Objective Function, -
\tilde{L}_a	Scaled Augmented Linearised Objective Function used for the adaptive thrust, -
M	Mach number, -
m	Vehicle mass = 550 kg

*MSc Graduate Student, Section Astrodynamics and Space Missions. guilledcalabuig@gmail.es

†Associate Professor, section Astrodynamics and Space Missions, e.mooij@tudelft.nl, Associate Fellow AIAA.

n_g	Normal load factor, -
R_{avr}	Earth radius Average radius = 6371000 m
R_e	Earth radius at equator = 6378137 m
R	Radial position, m
R_N	Vehicle Nose radius = 0.5 m
S_{ref}	Reference surface area = 2.408 m ²
t	Time, s
t_f	Final time, s
t_0	Initial time, s
q_c	Convective heat flux density, W/m ²
\mathbf{u}	Control vector, various
V	Groundspeed velocity, m s ⁻¹
\mathbf{x}	State vector, various
\mathbf{z}	Stacked optimisation variables, -
α	Angle of attack, rad or Step length, -
γ	Flight-path angle, rad
δ	Geocentric latitude, rad
η_α	Single-parameter defining angle-of-attack profile, rad
η	Radius of thrust region, m
χ	Heading angle, rad
ξ	Virtual Buffer Zone, -
λ	Longitude, rad or Penalty weight -
μ_E	Gravitational parameter of the Earth = $3.9859383624 \times 10^{14}$ m ³ /s ²
ν	Virtual control, -
ρ	Atmospheric density, kg/m ³
ρ_0	Earth surface density = 1.225 kg/m ³
σ	Bank angle, rad
τ	Pseudospectral time, -
ω_E	Earth angular velocity = $2\pi/86164.09054$ rad s ⁻¹

I. Introduction

Re-entry guidance is essential for space-transportation vehicles, as it determines the attitude commands to return safely from orbit. This is key for lifting vehicles, which can use their own aerodynamic surfaces to produce lift perpendicular to the velocity vector to reduce mechanical and aero-thermal loads, while providing manoeuvrability in terms of lift magnitude and direction to enable optimal re-entry and safe landing.

During the Apollo programme, the first generation of entry guidance methods were developed for low lift-to-drag (L/D) vehicles based on lift and drag acceleration control.^{1,2} This was shown to be robust to L/D variations and other perturbations,³ as accelerations could be provided directly by the inertial measurement unit simplifying the guidance, navigation and control (GNC) design. Designed for ballistic entries with nearly-constant angle of attack, bank-angle commands were generated to correct the predicted downrange error in combination with a bank reversal logic based on cross-range considerations. The methods were heavily constrained, relied strongly on semi-empirical relations due to the limited computational power available, and depended on a considerable number of assumptions. Consequently, the guidance approach lacked robustness and adaptability to a wider range of missions, which was required for the upcoming higher lift-to-drag vehicles.

With the development of the Space Transportation System (STS), the Apollo acceleration entry guidance was extended for higher L/D vehicles to exploit the increased manoeuvrability.⁴ It was later shown that more accurate trajectories could be generated if the drag-velocity plane was changed to the drag-energy plane.^{3,5,6} These algorithms only planned longitudinal motion,⁵⁻⁸ although extensions exist to account for lateral planning.^{3,9,10} The resulting entry guidance algorithms were suitable for on-board implementation. Nonetheless, assumptions such as small flight-path angles and quasi-equilibrium glide conditions (QEGC) limited their optimality and applicability.¹¹ Moreover, one of the major factors for tracking acceleration was the measurement inaccuracy of the navigational solution for altitude and velocity. Today's improved sensors

and navigation capabilities provided by the Global Positioning System allow for trajectories expressed in their natural state space,¹¹ providing larger information on the entry dynamics to meet strict specifications, reducing the necessity of direct acceleration tracking

Once a trajectory is planned, trajectory tracking algorithms can be used to correct for deviations caused by off-nominal conditions and modelling errors.^{3,16–19} Nevertheless, significant deviations can result in excessive guidance corrections and effort. To overcome these limitations, the third generation of guidance algorithms uses modern computational capabilities to enable a paradigm shift to generate real-time optimal and traceable trajectories in a robust guidance and control system.^{29,30} These may use acceleration and closed-form analytical solutions combined with predictor-corrector techniques^{10,11} or convex optimisation,²⁰ interpolation of optimal trajectories,^{24,25} predictor-corrector methods,^{8,26} and neural networks.²⁷ Pseudospectral optimisation could also provide real-time capabilities due to its fast convergence by solving the optimal control problem as a non-linear programming problem (NLP)¹² and correcting for errors produced by model uncertainties,^{31–34} but it demands high computational intensity, accurate initial estimates and, in general, it not possible to define an upper bound on the computational time.^{13,14}

Due to its high efficiency, guaranteed convergence, fast computational time and the current strong push towards automation in space operations, convex optimisation appears to be an indispensable technique for guidance navigation and control systems with real-time capable applications.^{21,35,36} Second-Order Cone Programming (SOCP) is a special case of convex optimisation, where highly efficient state-of-the-art numerical algorithms exist that can solve the problem within polynomial time,³⁷ such as the primal-dual interior-point method. In addition to the fast computational advantage, the solution is guaranteed to exist for a predetermined accuracy within an upper bound on the number of iterations.²³ Moreover, it does not require user-defined initial guesses as they use a self-dual embedding technique and can provide an adequate results when the problem is infeasible, an important safety requirements for adaptive guidance systems.

Many aerospace problems are inherently non-linear, in particular atmospheric re-entry, and considerable effort is required to re-formulate the problem. Methods to do so include lossless conversion and relaxations into a series of convex problems,^{21,23,39} or, when it is not possible, successive convex programming.^{15,40,41,43} In Refs. 39 and 23 the authors extended the rendezvous problem to address this by formulating the equations of motion with respect to energy, replacing the velocity equation for an approximation and applying a set of linearisations and relaxation techniques, resulting in an SOCP. The sequential approach has also been applied to reusable rockets returning to Earth⁴⁴ and gliding entry vehicles,^{22,45–47} and has been extended to free final time and angle of attack, assuming a polar aerodynamic database behaviour.^{48,49}

In this research, the original direct linearisation-based formulation used in Refs. 22 and 45, which optimised for bank angle, was adapted for the strict requirements of an optimal-based abort mission studied in Ref. 25, and compared with alternative lossless convexification possibilities. This requires an extension to include free final time and angle of attack in the optimisation loop, and the inclusion of higher-order environment assumptions. In addition, the successive convexification framework for atmospheric vehicles⁴⁷ is extended with a golden-section search algorithm, a virtual buffer zone on the heat-flux constraint is included, and different objective functions are compared to determine the characteristics and suitability for on-board planning. A preliminary, novel approach to design an angle-of-attack profile on a single parameter, which serves as a baseline for the comparison of successive convexification, is also presented. The resulting guidance planner is then used to assess the reachability capabilities of the SPHYNX vehicle, a scaled-down version of the X-38 lifting body, during orbital-abort and descent-abort scenarios.

This paper first describes the atmospheric re-entry problem, the SPHYNX vehicle and abort mission requirements in Sec. II. The general Successive Convex Optimal Control tool (SCOPT) developed and released under open license (<https://github.com/guidoca/scopt2>), and the golden-section search extensions are then presented in Sec. III. The different formulations for the atmospheric optimal control problem and its integration into a guidance planner are then described in Sec. IV. Sections V and VI give results of the analysis for different objectives and formulations, and the orbital and descent abort capabilities of the on-board planner. Section VII concludes the paper with final remarks and an outlook for future work.

II. Atmospheric Re-entry Problem and Abort Guidance Design

A. Equations of Motion and Simulation Model

The un-powered atmospheric re-entry problem can be formulated in spherical coordinates with the following equations of motion for a gravitational field with zonal components:⁵⁰

$$\dot{R} = \dot{h} = V \sin \gamma \quad (1)$$

$$\dot{\lambda} = \frac{V \sin \chi \cos \gamma}{R \cos \delta} \quad (2)$$

$$\dot{\delta} = \frac{V \cos \chi \cos \gamma}{R} \quad (3)$$

$$\dot{V} = -\frac{D}{m} + g_R \sin \gamma + g_\delta \sin \chi \cos \gamma + \omega_E^2 R \cos \delta (\sin \gamma \cos \delta - \cos \gamma \sin \delta \cos \chi) \quad (4)$$

$$\begin{aligned} \dot{\gamma} = & \frac{L \cos \sigma}{m V} + \frac{V}{R} \cos \gamma + \frac{g_R \cos \gamma}{V} - \frac{g_\delta \sin \chi \sin \gamma}{V} + 2\omega_E \cos \delta \sin \chi \\ & + \frac{\omega_E^2 R}{V} \cos \delta (\cos \delta \cos \gamma + \sin \gamma \sin \delta \cos \chi) \end{aligned} \quad (5)$$

$$\begin{aligned} \dot{\chi} = & \frac{L \sin \sigma}{m V \cos \gamma} + \frac{V}{R} \cos \gamma \tan \delta \sin \chi - \frac{g_\delta \sin \chi}{V \cos \delta} + 2\omega_E (\sin \delta - \cos \delta \cos \chi \tan \gamma) \\ & + \frac{\omega_E^2 R}{V \cos \gamma} \cos \delta \sin \delta \sin \chi \end{aligned} \quad (6)$$

where R is the radial position, h the geocentric altitude, λ the longitude, δ geocentric latitude, V the groundspeed modulus, γ the flight-path angle, χ the heading angle, and m the vehicle mass. ω_E represents the Earth rotation rate, whereas g_R and g_δ are the radial and meridional acceleration component, respectively:

$$g_R = -\frac{\mu}{R^2} \left[1 - \frac{3}{2} J_2 \left(\frac{R_e}{R} \right)^2 (3 \sin^2 \delta - 1) \right] \quad \text{and} \quad g_\delta = -3 \frac{\mu}{R^2} \left(\frac{R_e}{R} \right)^2 J_2 \sin \delta \cos \delta \quad (7)$$

The lift and drag forces, L and D , are given as:

$$L = \frac{1}{2} S_{ref} C_L(\alpha, M) \rho(h) V^2 \quad \text{and} \quad D = \frac{1}{2} S_{ref} C_D(\alpha, M) \rho(h) V^2 \quad (8)$$

where S_{ref} is the surface reference area, ρ is the atmospheric density dependent on altitude, C_L and C_D are the trimmed lift and drag coefficients, which depend on the vehicle Mach number and angle of attack. The atmospheric properties were computed assuming an ellipsoidal Earth with a geodetic altitude given as $h^* = R - R_{eq} (1 - f \sin^2 \delta)$. The geodetic altitude was also used to define the target final position which was approximated as $\delta^* = \delta + f \sin(2\delta)$. The SPHYNX lifting body was used, with an approximate L/D of 1.2 in supersonic and 2.0 in subsonic conditions, and with a nominal mission scenario towards the Azores Islands ($36.974^\circ, -25.165^\circ$) with the Entry Interface Point (EIP) condition as given in Table 1. The aerodynamic coefficients were computed using a spline interpolation from a trimmed, tabulated database, and its derivatives with respect to M and α used by the on-board guidance with a numerical central difference scheme. The L/D can be seen as a function of Mach and angle of attack in Fig. 1.

The trimmed database shows a highly non-convex aerodynamic behaviour, with complex angle of attack limits, especially during the transonic region. Re-entry vehicles usually fly with a pre-planned angle of attack to ensure adequate flying qualities, which motivated Wang and Grant⁴⁵ to synthesise a trajectory planner based on successive convexification with a given angle-of-attack profile. Nevertheless, there seems to be a large feasible space, which could be exploited during trajectory planning for a high degree of optimality.²⁴ Therefore, this research considered angle of attack as a possible control variable with different formulation options, as discussed in Sec. IV.B.

Table 1. SPHYNX nominal entry initial conditions⁵¹

Altitude	Longitude	Latitude	Velocity	Flight-path Angle	Heading Angle
120 km	-115°	30°	7643.7 m/s	-1.29°	43.04°

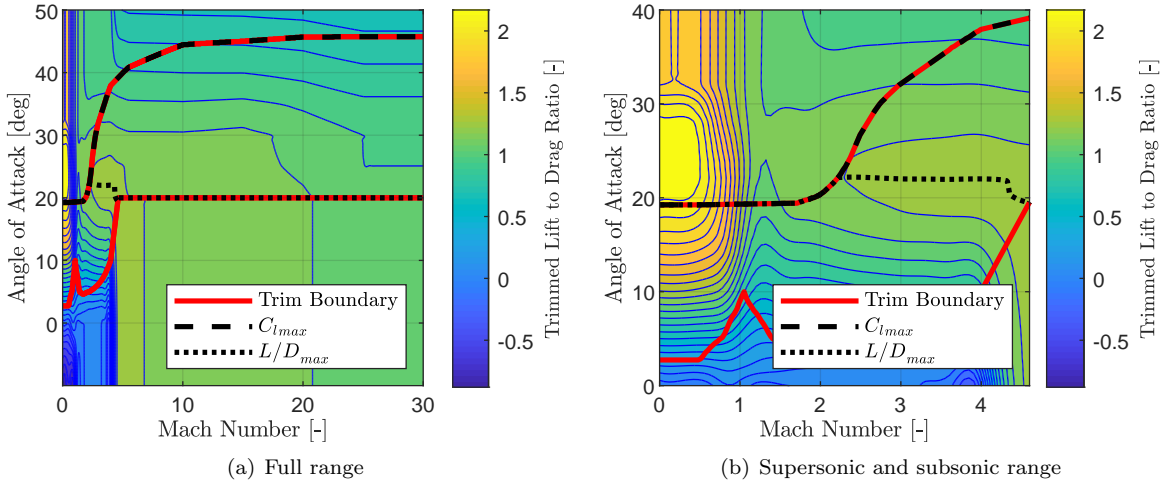


Figure 1. Lift-to-Drag of the trimmed aerodynamics; the red line determines the maximum and minimum boundaries

B. Entry Corridor

The re-entry trajectory is constrained by the so-called entry corridor based on a set of operational requirements. In the current research, we consider a heat-flux and aerodynamic-load constraint as follows:

$$q_{c_{max}} \geq q_c = g_1(R, V) = \frac{c^*}{R_N^n} \left(\frac{\rho(h)}{\rho_0} \right)^{1-n} \left(\frac{V}{V_c} \right)^m \quad (9)$$

$$n_{g_{max}} \geq n_g = g_2(R, V, \alpha) = \frac{\rho(h) V^2 S_{ref}}{2m g_0} \sqrt{C_D^2(\alpha, M) + C_L^2(\alpha, M)} \quad (10)$$

where $c^* = 1.1097 \times 10^8 \text{ m}^{1/2}$, $\rho_0 = 1.225 \text{ kg/m}^3$, $V_c = 7905.4 \text{ m/s}$, R_N is the vehicle nose radius, typically $m = 3$ for a viscosity proportional to the square root of the absolute temperature and in-compressible flow from the bow shock to the stagnation point, and $n = 0.5$ for laminar boundary layers. Additional constraints, such as a dynamic-pressure limit, temperature limits, and bending moments may be imposed to define the entry corridor, but were not considered given the mission requirements as described in Ref. 51. Although the heat load could also be included as a hard limit, it was considered as a possible guidance metric.

III. Successive Convex Optimisation for Rapid On-board Planning

The entry guidance analysed in this research plans the trajectory using optimal control via successive convexification. This section describes the approach followed to synthesise the generalised Successive Convex Optimal Control tool and its extensions. For specific details, the reader can consult Ref. 51.

A. Optimal Control Problem Formulation

The optimal on-board planning guidance algorithm solves the optimal control problem of the Bolza type:

$$J(t_0, t_f, \mathbf{x}, \mathbf{u}) = \mathfrak{M}[t_0, t_f, \mathbf{x}(t_0, t_f), \mathbf{u}(t_0, t_f)] + \int_{t_0}^{t_f} \mathcal{L}[\mathbf{x}(t), \mathbf{u}(t)] dt \quad (11)$$

where $J(t_0, t_f, \mathbf{x}, \mathbf{u}) : \mathbb{R} \times \mathbb{R} \times \mathbb{R}^{n_x} \times \mathbb{R}^{n_u} \rightarrow \mathbb{R}$ is the objective function, $\mathbf{x}(t) \in \mathbb{R}^{n_x}$, represents the state trajectory $\mathbf{u}(t) \in \mathbb{R}^{n_u}$, the control inputs, $\mathfrak{M}[t_0, t_f, \mathbf{x}(t_0, t_f), \mathbf{u}(t_0, t_f)] : \mathbb{R} \times \mathbb{R} \times \mathbb{R}^{n_x} \times \mathbb{R}^{n_u} \rightarrow \mathbb{R}$ is the Mayer term and $\mathcal{L}[\mathbf{x}(t), \mathbf{u}(t)] : \mathbb{R}^{n_x} \times \mathbb{R}^{n_u} \rightarrow \mathbb{R}$ is the Lagrange term. The initial time was considered to be $t_0 = 0$ without loss of generality.

The equations of motion are implemented as equality constraints and are assumed time independent:

$$\frac{d\mathbf{x}}{dt} = \mathbf{f}(\mathbf{x}(t), \mathbf{u}(t)) \quad (12)$$

where $\mathbf{f} : \mathbb{R}^{n_x} \times \mathbb{R}^{n_u} \rightarrow \mathbb{R}^{n_x}$ is a control-state non-linear mapping function. The state, control and time variables are constraint by the following bounds:

$$\mathbf{x}_l \leq \mathbf{x}(t) \leq \mathbf{x}_u \quad , \quad \mathbf{u}_l \leq \mathbf{u}(t) \leq \mathbf{u}_u \quad , \quad t_{f_l} \leq t_f \leq t_{f_u} \quad (13)$$

The initial and final conditions can be accounted for as inequality event constraints as follows:

$$e_l \leq e(\mathbf{x}(t_0, t_f), \mathbf{u}(t_0, t_f)) \leq e_u \quad (14)$$

where $e(t_0, t_f) : \mathbb{R}^{n_x} \times \mathbb{R}^{n_u} \rightarrow \mathbb{R}$ is the mapping function which represents the event constraint and can be assumed as non-linear.

In addition, the problem can include the following path constraints

$$g_l \leq g(\mathbf{x}(t), \mathbf{u}(t)) \leq g_u \quad (15)$$

where $\mathbf{g}(t) : \mathbb{R}^{n_x} \times \mathbb{R}^{n_u} \rightarrow \mathbb{R}$ represents the path constraint mapping function, which in the case of linear path constraint.

Pseudo-spectral time was used to include the time of flight as an additional optimisation variable, $\tau = \frac{2}{t_f - t_0} t - \frac{t_f + t_0}{t_f - t_0}$, obtaining the following different equations for the objective:

$$J = \mathfrak{M}[t_0, t_f, \mathbf{x}(-1, 1), \mathbf{u}(-1, 1)] + \frac{(t_f - t_0)}{2} \int_{-1}^1 \mathfrak{L}[\mathbf{x}(\tau), \mathbf{u}(\tau)] d\tau \quad (16)$$

and dynamics:

$$\frac{d\mathbf{x}}{d\tau} = \frac{(t_f - t_0)}{2} \mathbf{f}(\mathbf{x}(\tau), \mathbf{u}(\tau)) \quad (17)$$

with the derivative path constraints now being expressed as:

$$g_l \frac{(t_f - t_0)}{2} \leq \frac{dg(\mathbf{x}(\tau), \mathbf{u}(\tau))}{d\tau} \leq \frac{(t_f - t_0)}{2} g_u \quad (18)$$

B. Successive Convexification

In this research, convex optimisation, specifically Second-Order Cone Programming problem (SOCP), was used to solve optimal control problem. The SOCP can be formulated as:

$$\min_{\mathbf{z}} \mathbf{f}^T \mathbf{z} \quad (19)$$

$$\text{Subject to: } \mathbf{M}^{eq} \mathbf{z} = \mathbf{p}^{eq} \quad (20)$$

$$\text{And: } \|\mathbf{A}_i^T \mathbf{z} + \mathbf{b}_i^T\|_2 \leq \mathbf{C}_i^T \mathbf{z} + \mathbf{d}_i \quad i = 1, \dots, m \quad (21)$$

where \mathbf{z} is the optimisation vector and Eq. (19) the performance index, subject to the equality constraints given by Eq. (20).

The (non-convex) entry dynamics can be formulated as a series of SOCPs and solved with interior-point solvers. This is performed by approximating the equations of motion, constraints and objective function with Taylor series expansions around the previous solutions to obtain affine and convex constraints. As a result, the problem becomes dependent on the initial guess and it may lose some of its computational advantages. During this research, it was seen that the atmospheric re-entry guidance presented in Ref. 45 was sensitive to the initial guess and augmentations were necessary to increase convergence,⁴⁷ especially when considering the highly constrained angle-of-attack corridor discussed in Sec. II.A.

To ensure that the problem remains feasible and to guarantee convergence, virtual controls, virtual buffers, adaptive thrust regions and line search routines were introduced. In Ref. 40 a technique based on successive convexification is developed, where the convex thrust-region-constraint is directly incorporated to the convex sub-problem, which is solved to full optimality. This method was incorporated in SCOPT and was also used for the adaptive on-board guidance because of its simple implementation and extensive use throughout the literature.^{15, 30, 40, 41, 47, 56}

C. Adaptive Thrust Regions

Refs. 40 and 41 proposed an adaptive thrust region algorithm analogous to moving limit algorithms for sequential linear programming.⁵³ In addition, it was extended to include non-linear constraints with virtual buffer zones. In Ref. 42 a modification for soft thrust regions is discussed, see also Refs. 38 and 40. The algorithm imposes a hard thrust region on the control constraints, which is updated at each iteration by measuring the convexification error with the following ratio:

$$\rho^k = \frac{\Delta \hat{J}_a^k}{\Delta \hat{L}_a^k} = \frac{\hat{J}_a^{k-1} - \hat{J}_a^k}{\hat{J}_a^{k-1} - \hat{L}_a^k} \quad (22)$$

where $\Delta \hat{J}_a^k = \hat{J}_a^{k-1} - \hat{J}_a^k$ is the actual change in the augmented objective function, and $\Delta \hat{L}_a^k = \hat{J}_a^{k-1} - \hat{L}_a^k$ is the predicted change by the convexified objective function. The subscript a means that it refers to the augmented non-convex and convex objective functions defined by Eqs. (27) and (28). The parameter ρ^k is compared with three values $0 \leq \rho_0 \leq \rho_1 \leq \rho_2 \leq 1$ as explained in Ref. 51.

D. Virtual Controls and Buffer Zones

Virtual controls can be augmented⁴⁰ augmented into the objective function, as explained in Sec. III.E, to prevent artificial infeasibility by introducing virtual controls as for the Euler discretisation:

$$\mathbf{x}_{i+1} = \mathbf{x}_i + \frac{\Delta\tau}{2} \left(\mathbf{f}_i^{k-1} t_f + (t_f^{k-1} - t_0) \mathbf{A}_i^{k-1} \mathbf{x}_i + (t_f^{k-1} - t_0) \mathbf{B}_i^{k-1} \mathbf{u}_i + \mathbf{h}_i^{k-1} \right) + \frac{\Delta\tau}{2} (t_f^0 - t_0) \mathbf{E} \boldsymbol{\nu}_i \quad (23)$$

where $\boldsymbol{\nu}_i \in \mathbb{R}^{n_{vc}}$ $\mathbf{E} : \mathbb{R}^{n_x \times n_{vc}}$ is defined to ensure that all states are reachable. Note that the virtual controls are multiplied by a term $\frac{\Delta\tau}{2} (t_f^0 - t_0)$, which is dependent on the initial guess of the final time.

Some highly non-convex path constraints as the heat flux can result in infeasible problems when being approximated. To account for this, Ref. 41 introduced artificial buffer zones to augment the constraint into the objective function:

$$e^{k-1} + (e_{\mathbf{x}}^{k-1})^T (\mathbf{x} - \mathbf{x}^{k-1}) + (e_{\mathbf{u}}^{k-1})^T (\mathbf{u} - \mathbf{u}^{k-1}) - \xi_e \leq e_u \quad (24)$$

with ξ_e for event and ξ_g for path virtual buffer zones.

E. Augmented Objective function

The augmented convex objective function is then given as:

$$\begin{aligned} \text{CP2: } L_a = & L + \lambda_{t_f} \left| t_f^k - t_f^{k-1} \right| + \lambda_y P_y^i [P_y^c (\mathbf{y}^k - \mathbf{y}^{k-1})] + \lambda_\nu P_\nu^i [P_\nu^c (\mathbf{E} \boldsymbol{\nu})] \\ & + \sum_{j=0}^{n_{\xi,g}} \lambda_{g,j} P_g^i [\max(0, \xi_{g,j})] + \sum_{j=0}^{n_{\xi,e}} \lambda_{e,j} \max(0, \xi_{e,j}) \end{aligned} \quad (25)$$

Equation (25) represents a convex objective function, but it still has to be represented in SOCP-feasible formulation. This is done by formulating the objective function CP3, or L , as:

$$\text{CP3: } L = s_L + \lambda_{t_f} \eta_{t_f} + \lambda_y \eta^{P2} + \lambda_\nu \nu^{P2} + \sum_{j=0}^{n_{\xi,g}} \lambda_{g,j} \xi_{g,j}^{P2} + \sum_{j=0}^{n_{\xi,e}} \lambda_{e,j} \xi_{e,j}^{P1} \quad (26)$$

and including the additional inequality constraint $L_a \leq s_L$. The adaptive thrust region metric function ρ uses different augmented objective formulations, which are given as:

$$\begin{aligned} \text{P2: } \hat{J}_a = & J + \lambda_{t_f} \left| t_f^k - t_f^{k-1} \right| + \lambda_y P_y^i [P_y^c (\mathbf{y}^k - \mathbf{y}^{k-1})] + \lambda_\nu P_d^i \left[P_d^c \left(\mathbf{x}_{i+1}^k - \mathbf{x}_i^k - \frac{\Delta\tau_i}{2} (t_f^k - t_0) \tilde{\mathbf{f}}_i^k \right) \right] \\ & + \sum_{j=0}^{n_g} \lambda_g^j P_g^i [\max(0, \tilde{\mathbf{g}}^{j,k})] + \sum_{j=0}^{n_e} \lambda_e^j \max(0, \tilde{e}^{j,k}) \end{aligned} \quad (27)$$

$$\begin{aligned}
\text{CP4: } \hat{L}_a = & L + \lambda_{tf} \left| t_f^k - t_f^{k-1} \right| + \lambda_y P_y^i [P_y^c (\mathbf{y}^k - \mathbf{y}^{k-1})] \\
& + \lambda_f P_d^i \left[P_d^c \left(\mathbf{x}_{i+1}^k - \mathbf{x}_i^k - \frac{\Delta \tau_i}{2} \left(\tilde{\mathbf{f}}_i^{k-1} t_f^k + (t_f^{k-1} - t_0) \left(\tilde{\mathbf{A}}_i^{k-1} \tilde{\mathbf{x}}^k + \tilde{\mathbf{B}}_i^{k-1} \tilde{\mathbf{u}}^k \right) + \tilde{\mathbf{h}}_i^{k-1} \right) \right) \right] \\
& + \sum_{j=0}^{n_g} \lambda_g^j P_g^i \left[\max(0, \tilde{\mathbf{g}}^{j,k} + \tilde{\mathbf{g}}_x^{j,k} (\tilde{\mathbf{x}}^k - \tilde{\mathbf{x}}^{k-1}) + \tilde{\mathbf{g}}_u^{j,k} (\tilde{\mathbf{u}}^k - \tilde{\mathbf{u}}^{k-1})) \right] \\
& + \sum_{j=0}^{n_e} \lambda_e^j \max(0, \tilde{e}^{j,k} + \tilde{e}_x^{j,k} (\tilde{\mathbf{x}}^k - \tilde{\mathbf{x}}^{k-1}) + \tilde{e}_u^{j,k} (\tilde{\mathbf{u}}^k - \tilde{\mathbf{u}}^{k-1}))
\end{aligned} \tag{28}$$

F. Line Search Method Based on Golden Section Search

In line-search methods, instead of directly solving for the magnitude and direction, a search direction is computed at each iteration $\mathbf{p} = \mathbf{z}^k - \mathbf{z}^{k-1}$, which then serves to move towards the optimum $\mathbf{z}^k = \mathbf{z}^{k-1} + \alpha \mathbf{p}$ by multiplying the search direction by a specific parameter α . This parameter can be computed by performing a single-parameter optimisation on α , as with a polynomial or cubic approximation of the objective function and using the Newton method,⁵⁴ or by satisfying the sufficient decrease condition.^{28,47} In this research, a golden section algorithm was used, as it did not require derivative information and a pre-defined number of iterations could be imposed. The algorithm is based on the Intermediate Value Theorem, which states that given a continuous function $M(\alpha)$ and an interval of $\alpha \in (\alpha_1, \alpha_4)$, a root is guaranteed to exist if the results of $M(\alpha) \leq M(\alpha_1)$ and $M(\alpha) \leq M(\alpha_4)$ are satisfied. The next step is to locate two new points, α_2 and α_3 according to a logical process. The golden section locates these new points as:

$$\alpha_2 = \alpha_1 + (1 - \Phi) (\alpha_4 - \alpha_0) \quad \text{and} \quad \alpha_3 = \alpha_1 + \Phi (\alpha_4 - \alpha_0) \tag{29}$$

where $\Phi = \frac{\sqrt{5}-1}{2} \approx 0.618$. In this application, it is assumed that $\alpha_1 = 0$ and $\alpha_4 = 1$. The algorithm then evaluates the merit function at $M(\alpha_1)$ and $M(\alpha_2)$. If the mid-points are such that $M(\alpha_1) \leq M(\alpha_2)$, then the optimum is in $[\alpha_0, \alpha_2]$ and $\{\alpha_0, \alpha_1, \alpha_2\}$ defines the initial triplet. On the other hand, if $M(\alpha_1) \geq M(\alpha_2)$, then $\{\alpha_1, \alpha_2, \alpha_3\}$ define the initial triplet. The algorithm then updates the triplet with the new mid-points α_2^n and α_3^n , Eq. (29), noticing that $\alpha_3^n = \alpha_2$ in the first case, and $\alpha_2^n = \alpha_3$ in the second case because of the golden section special properties. This sequence is repeated n times until a desired tolerance $\alpha_1 - \alpha_4 \leq \epsilon_g$ is met, which can be computed beforehand. The merit function $M(\alpha)$ used is based on the augmented non-convex objective function defined by P2 in Eq. (27) evaluating the resulting \mathbf{z}^k from the step length update. As it is desired to leave the bulk of the solution to the SOCP solver, a small tolerance resulting from $n = 5$ steps was used.

IV. On-board Abort Re-entry Guidance Planning via Successive Convexification

This section presents the various atmospheric re-entry successive convexification algorithm formulations and their implementation into the guidance planner using the successive convexification framework presented in the previous sections. The algorithm extends the fixed time of flight and angle of attack problem formulations^{22,23,45,47} to free final time problems and angle of attack control.

A. Preliminary Angle-of-Attack and Bank-Angle Planning

During the development of the successive convexification algorithm for the atmospheric re-entry problem, it was observed that, although for some problems a non-feasible trivial initial guess strategy connecting the initial and final conditions could be successful, a robust guess was required to guarantee higher convergence rates and reduce control chattering. This was also motivated by the highly non-linear constraints in the α -Mach corridor for the aerodynamic database seen in Sec. II.A. Nevertheless, it was observed that simple angle-of-attack and bank-angle control laws with constant or linear profiles resulted in adequate initial guesses when using virtual controls and a heat flux buffer zone. This was also the case, when the angle of attack was outside of the trimming boundaries and the altitude-velocity trajectory violated the heat-flux constraint.

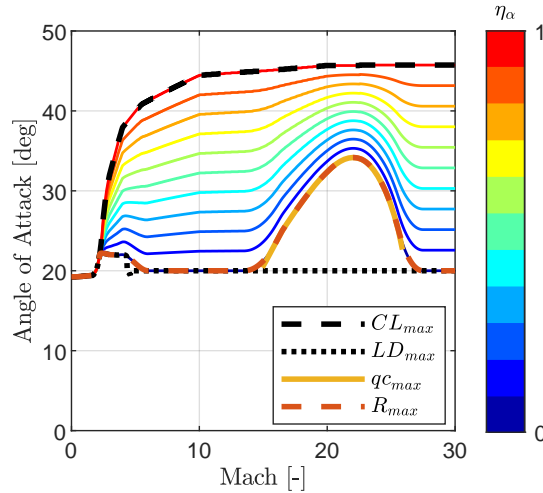


Figure 2. Designed angle of attack planning law for different η_α values with a spacing of 0.1,

The approach followed is based on the quasi-equilibrium glide condition given by:

$$\frac{1}{2}\rho(h)V^2 S_{ref} C_L(V, h) \sin(\sigma_{min}) - m \left[g(h) - \frac{V^2}{R(h)} \right] = 0 \quad (30)$$

For the preliminary bank-angle control law, feedback linearisation with the QEGC was used with a proportional gain.^{51, 52} The QEGC was also used to translate any trajectory point from the altitude-velocity to the angle-of-attack and Mach number plane. Two profiles were defined as interpolation limits as in Ref. 52, one for the minimum range corresponding to the maximum C_L , and another one for maximum range corresponding to a combination of the maximum L/D constrained by the heat-flux limit,⁵¹ as in Fig. 2.

The maximum range angle-of-attack profile, $\alpha_{R_{max}}(M)$, was computed by using the maximum value between $\alpha_{qc_{max}}(M)$ and $\alpha_{L/D_{max}}(M)$. To remove discontinuities derived from the integration of both profiles and from the discontinuous $\alpha_{L/D_{max}}(M)$ profile, a third-order polynomial was used matching the derivative information at every intersection, together with an interpolation law on a single parameter η_α as follows:

$$\alpha(M) = \alpha_{C_L^{max}}(M) \eta_\alpha + \alpha_{R_{max}}(M) (1 - \eta_\alpha) \quad (31)$$

B. Basic Successive Convexification for Atmospheric Re-entry

The re-entry optimisation problem used spherical coordinates for position and velocities. In this formulation, only bank-angle control was assumed to reduce the problem size, while angle of attack is directly provided as a function of Mach number for a given η_α as discussed in Sec. IV.A. The state and control vectors are therefore:

$$\mathbf{x}(t) = [R(t), \delta(t), \lambda(t), V(t), \gamma(t), \psi(t)] \quad , \quad \mathbf{u}(t) = \sigma(t) \quad (32)$$

with the equations of motion, defined in spherical coordinates as in Eqs. (1) to (6), and stacked as:

$$\dot{\mathbf{x}} = \mathbf{f}(\mathbf{x}, \mathbf{u}) \quad (33)$$

This dynamics is highly non-linear and requires a linearisation for compatibility with convex problems. If this was done directly, the linearised dynamics would become dependent on previous bank-angle solutions, which can produce high frequency chattering associated to numerical instabilities, a typical issue found in many non-linear programming problems based on sequential optimisation. This can detriment the problem's convergence,²³ and was also noted to appear in powered landing problems.^{38, 42}

An additional state equation for the bank angle can be introduced to mitigate this issue,⁴⁵ as it was found that using rates as optimisation variables improved the convergence and performance of the sequential method. Furthermore, it allows to directly limit the bank-angle rate of change and capture the dynamics

associated to bank-angle reversal considerations during trajectory planning. This augments the state vector and equations of motion as follows:

$$\dot{\sigma} = u_1(t) \quad , \quad \mathbf{x}(t) = [R(t), \delta(t), \lambda(t), V(t), \gamma(t), \psi(t), \sigma(t)] \quad , \quad \mathbf{u}(t) = u_1(t) \quad (34)$$

which decouples the state and control variables from the equations of motion as shown for the decomposed state vector

$$\dot{\mathbf{x}} = \mathbf{f}(\mathbf{x}, \mathbf{u}) = \mathbf{f}_0(\mathbf{x}) + \mathbf{B}\mathbf{u} + \mathbf{f}_\omega(\mathbf{x}) \quad (35)$$

where \mathbf{f}_ω includes the rotation dependent terms of the equation of motion. The bank angle, and the rate limit for bank angle can then be constrained as:

$$-\sigma_{max} \leq \sigma \leq \sigma_{max} \quad \text{and} \quad \dot{\sigma}_{max} \leq \dot{\sigma} \leq \dot{\sigma}_{max} \quad (36)$$

In addition to the choice of coordinate systems, optimisation variables and time of flight treatment, an additional technique is to use lossless convexification. The method transforms the non-convex functions into second-order cone form, which allows to compute the global minimum of a problem in deterministic time.²¹ This may be done in many aerospace applications, and although it does not always lead to a fully convex problem, it may reduce the convergence difficulties for some problems associated to non-linearities.⁵⁵

For re-entry applications, a lossless convexification of the bank-angle control can be performed by introducing a regularisation term as a function of the heading angle.^{23,55} The resulting state vector, \mathbf{x} , is as given by Eq. (32), while the control vector is:

$$\mathbf{u}(t) = (u_1, u_2) \quad (37)$$

where

$$u_1 = \cos \sigma \quad \text{and} \quad u_2 = \sin \sigma \quad (38)$$

which requires the introduction of the following equality constraint containing the non-linearities:

$$\sqrt{u_1^2 + u_2^2} = 1 \quad (39)$$

This modifies the state derivatives for the flight-path angle and heading angle, Eqs. (5) and (6):

$$\dot{\gamma} = \frac{L'u_1}{V} + \frac{\cos \gamma}{V} \left(\frac{-\mu}{R^2} + \frac{V^2}{R} \right) + 2\omega_E \cos \delta \sin \chi + \omega_E^2 \frac{R}{V} \cos \delta (\cos \delta \cos \gamma + \sin \gamma \sin \delta \cos \chi) \quad (40)$$

$$\dot{\chi} = \frac{L'u_2}{V \cos \gamma} + \frac{V}{R} \cos \gamma \tan \delta \sin \chi + 2\omega_E (\sin \delta - \cos \delta \tan \gamma \cos \chi) + \omega_E^2 \frac{R}{V \cos \gamma} \cos \delta \sin \delta \sin \chi \quad (41)$$

Equation (39) is not a convex constraint, as it is defined with the equivalent sign. To introduce it as a second-order cone, the equality sign has to be relaxed into a lower or equal constraint as:

$$\sqrt{u_1^2 + u_2^2} \leq 1 \quad (42)$$

This relaxation also allows to include a minimum bank-angle magnitude constraint as:

$$\cos(|\sigma|_{min}) \geq u_1 \quad (43)$$

which is adequate for tracking purposes to allow for sufficient bank-angle controllability at nearly zero banking, and requires the modification of the σ boundaries as:

$$\cos(|\sigma|_{max}) \leq u_1 \quad \text{and} \quad -\sin(|\sigma|_{max}) \leq u_2 \leq \sin(|\sigma|_{max}) \quad (44)$$

As a result of this lossless relaxation, Eq. (39) might not be met in many optimum solutions, although it can be guaranteed if the following term is augmented into the objective function:²³

$$\mathfrak{R} = \lambda_\chi \int_{t_0}^{t_f} \chi dt \quad (45)$$

This regularisation term is a function of the integral of the heading angle χ and required a sign-selection logic for λ_χ , which was empirically seen in Ref. 23. It could be selected based on the landing-site location,

as if it required to bank counterclockwise in north direction (positive sign) or clockwise in south direction. In addition, the magnitude for λ_χ had to be selected by trial and error to not shadow the original function, while still guaranteeing Eq. (39).

A problem with this formulation is that it does not allow for bank-angle rate limits. It is also seen that this convexification does not fully decouple the state and control variables from the equations of motion. To overcome this, Ref. 23 used the energy domain, approximating the velocity equation with a relation based on energy. Although the domain might be suitable for re-entry optimisation problems, as it better captures its dynamics, it was decided to transform this lossless approach to the time domain to better compare both approaches and omit the flight-path angle approximation. This was seen to be considerably high during the final portions of the re-entry as speeds of less than Mach one were reached and high accuracy to meet the Descent and Recovery System (DRS) constraints is required.

The SCOP formulation, Eq. (21), only allows for affine equality constraints. Therefore, it is necessary to linearise the equations of motion, requiring analytical derivations of the state \mathbf{A} and control \mathbf{B} matrices. Nevertheless, it is not necessary to include small terms, as can be the case of higher-order gravitational effects, the ellipsoidal Earth shape and the Earth's rotational rate. Therefore, although these can be included in the state-derivatives, it is not necessary to include them in the state-transition matrix.

For the direct linearisation approach, the state and control matrices without the rotational derivatives are given as:

$$\mathbf{A}(\mathbf{x}) = \begin{bmatrix} 0 & 0 & 0 & a_{RV} & a_{R\gamma} & 0 & 0 \\ a_{\lambda R} & 0 & a_{\lambda\delta} & a_{\lambda V} & a_{\lambda\gamma} & a_{\lambda\chi} & 0 \\ a_{\delta R} & 0 & 0 & a_{\delta V} & a_{\delta\gamma} & a_{\delta\chi} & 0 \\ a_{VR} & 0 & 0 & a_{VV} & a_{V\gamma} & 0 & 0 \\ a_{\gamma R} & 0 & 0 & a_{\gamma V} & a_{\gamma\gamma} & 0 & a_{\gamma\sigma} \\ a_{\chi R} & 0 & a_{\chi\delta} & a_{\chi V} & a_{\chi\gamma} & a_{\chi\chi} & a_{\chi\sigma} \\ 0 & 0 & 0 & 0 & 0 & 0 & 0 \end{bmatrix}, \quad \mathbf{B} = \begin{pmatrix} 0 \\ 0 \\ 0 \\ 0 \\ 0 \\ 0 \\ 1 \end{pmatrix} \quad (46)$$

while for the lossless convexification approach the state and control matrices are:

$$\mathbf{A}(\mathbf{x}, \mathbf{u}) = \begin{bmatrix} 0 & 0 & 0 & a_{RV} & a_{R\gamma} & 0 \\ a_{\lambda R} & 0 & a_{\lambda\delta} & a_{\lambda V} & a_{\lambda\gamma} & a_{\lambda\chi} \\ a_{\delta R} & 0 & 0 & a_{\delta V} & a_{\delta\gamma} & a_{\delta\chi} \\ a_{VR} & 0 & 0 & a_{VV} & a_{V\gamma} & 0 \\ a_{\gamma R} & 0 & 0 & a_{\gamma V} & a_{\gamma\gamma} & 0 \\ a_{\chi R} & 0 & a_{\chi\delta} & a_{\chi V} & a_{\chi\gamma} & a_{\chi\chi} \end{bmatrix}, \quad \mathbf{B}(\mathbf{x}) = \begin{bmatrix} 0 & 0 \\ 0 & 0 \\ 0 & 0 \\ 0 & 0 \\ b_{\gamma u_1} & 0 \\ 0 & b_{\chi u_2} \end{bmatrix} \quad (47)$$

where the matrix components a_{ij} can be found in Ref. 51. The terms a_{VR} , a_{VV} , $a_{\gamma R}$, $a_{\gamma V}$, $a_{\chi R}$, $a_{\chi V}$, $b_{\gamma u_1}$ and $b_{\chi u_2}$ are also a function of the derivatives of the aerodynamic coefficients. In Refs. 15, 22, 45 and 47, these were assumed to be Mach independent and only a function of angle of attack, such that, although it was speed dependent, it was assumed to independent: $\frac{d\alpha}{dV} \approx 0$. The former condition may hold in the high hypersonic regime, but it may not capture the supersonic and transonic dynamics during the final re-entry portions, where high precision is required to meet the DRS conditions.

The path constraints on heat flux and normal load, Eqs. (9) and (10), are linearised as follows:

$$q_c(R, V) := q_c(R^{k-1}, V^{k-1}) + q_{cR}(R^{k-1}, V^{k-1})(R - R^{k-1}) + q_{cV}(R^{k-1}, V^{k-1})(V - V^{k-1}) \leq q_{cmax} \quad (48)$$

$$n_g(R, V) := n_g(R^{k-1}, V^{k-1}) + n_{gR}(R^{k-1}, V^{k-1})(R - R^{k-1}) + n_{gV}(R^{k-1}, V^{k-1})(V - V^{k-1}) \leq n_{gmax} \quad (49)$$

where q_{cR} , q_{cV} , n_{gR} and n_{gV} are the respective Jacobians, given as:

$$q_{cR} = \frac{\partial q_c(R, V)}{\partial R} = \frac{c^*}{R_N^n \rho_0^{1-n}} (1-n) (\rho(h))^{-n} V^m \frac{d(\rho(h))}{dh} \quad (50)$$

$$q_{cV} = \frac{\partial q_c(R, V)}{\partial V} = \frac{c^*}{R_N^n \rho_0^{1-n}} (\rho(h))^{1-n} m V^{m-1} \quad (51)$$

for the heat flux, and:

$$n_{gR} = \frac{\partial n_g(R, V)}{\partial R} = \frac{S_{ref}}{2m_{sc}} V^2 \left(\sqrt{C_L^2 + C_D^2} \frac{d(\rho(h))}{dh} - \frac{\rho(h) V}{a(h)^2} \frac{da}{dh} \frac{(C_L \frac{dC_L}{dM} + C_D \frac{dC_D}{dM})}{\sqrt{C_L^2 + C_D^2}} \right) \quad (52)$$

$$n_{gV} = \frac{\partial n_g(R, V)}{\partial V} = \frac{S_{ref}}{2m_{sc}} \rho(h) \left(2V \sqrt{C_L^2 + C_D^2} + \frac{V^2}{a(h)} \frac{(C_L \frac{dC_L}{dM} + C_D \frac{dC_D}{dM})}{\sqrt{C_L^2 + C_D^2}} \right) \quad (53)$$

for the normal load.

A fixed step collocation method using trapezoidal discretisation was considered to provide sufficiently accurate solutions and selected for the analysis. The time was discretised as $t_i = t_f/N - 1$ with t_f representing the time to go. The initial number of nodes and discretisation step could be chosen directly, although a more convenient approach with free final time problems or those using virtual controls was to propagate until a maximum time or DRS conditions were met with a small initial time step of 5 s and use the resulting states histories and number of nodes with the specific initial guess final time.

C. Extended Successive Convexification for Atmospheric Re-entry

The basic successive convexification algorithm described in Sec. IV.B had been previously used for an on-board optimal control based guidance.⁴⁵ Nevertheless, a number of extensions had to be implemented for the SPHYNX vehicle abort-guidance design to satisfy the requirements described in Ref. 51 and to include the tabulated aerodynamic database with non-convex constraints.

The original problem formulation described in Refs. 15, 22, 45 and 47 considered a fixed time of flight problem as a proof of concept. Nonetheless, it is difficult to estimate an adequate initial guess for the final time and an abort mission can have a large envelope of situations as was seen in Ref. 25, depending on the EIP, landing site, and abort condition. Free time of flight was already incorporated for atmospheric re-entry problem formulation with a flat earth approach and approximating the aerodynamics with a polar approximation.^{48, 49}

Different approaches to include angle of attack in the optimisation process were analysed in Ref. 51. A polar approximation did not capture the re-entry aerodynamics of the lifting body in the hypersonic region and was therefore not included in the comparison. It was seen that adequate results were obtained if the angle of attack rates were optimised directly. By doing so, a direct linearisation on angle of attack was necessary, as explained in Sec. IV.B for the bank angle. This mitigated control chattering, while allowing to implement bounds directly on its derivative. Furthermore, it can be combined with the direct bank-angle rate optimisation or the lossless convexification of bank-angle approach, which was called the *hybrid* method throughout the study.

Therefore, in the case of direct angle-of-attack and bank-angle optimisation, the augmented dynamics, state and control vector are defined as follows:

$$\mathbf{x}(t) = [R(t), \delta(t), \lambda(t), V(t), \gamma(t), \psi(t), \sigma(t), \alpha(t)] \quad , \quad \mathbf{u}(t) = [u_1(t), u_2(t)] \quad (54)$$

with

$$\dot{\sigma} = u_1(t) \quad \text{and} \quad \dot{\alpha} = u_2(t) \quad (55)$$

This keeps the decoupling of states and controls, *i.e.*, in the format of Eq. (35); details on the new state and control matrices, $\mathbf{A}(\mathbf{x})$ and \mathbf{B} , can be found in Ref. 51.

An alternative formulation using a lossless bank angle was also analysed with, states and control vector are defined as:

$$\mathbf{x}(t) = [R(t), \delta(t), \lambda(t), V(t), \gamma(t), \psi(t), \alpha(t)] \quad , \quad \mathbf{u}(t) = [u_1(t), u_2(t), u_3(t)] \quad (56)$$

with

$$\dot{\alpha} = u_3(t) \quad (57)$$

where u_1 and u_2 are defined by Eq. (38).

Furthermore, the normal load constraint contained an additional derivative to Eqs. (52) and (53):

$$n_{g\alpha} = \frac{\partial n_g(R, V)}{\partial \alpha} = \frac{S_{ref}}{2m_{sc}} \rho V^2 \left(\frac{C_L \frac{dC_L}{d\alpha} + C_D \frac{dC_D}{d\alpha}}{\sqrt{C_L^2 + C_D^2}} \right) \quad (58)$$

and the angle of attack trimming boundaries for accurate flying qualities described in Sec. II imposed the following path constraints on angle of attack which were function of the Mach Number:

$$\alpha_{Lower}(M) \leq \alpha \leq \alpha_{Upper}(M) \quad (59)$$

These constraints were linearised as functions of previous radius R^{k-1} and ground-speed V^{k-1} states as shown for the following generalised constraint α_{lim} :

$$\alpha_{lim}(R, V) = \alpha_{lim}(R^{k-1}, V^{k-1}) - \frac{d\alpha_{lim}}{dM} \frac{\rho(h)V}{a(h)^2} \frac{da}{dh} (R - R^{k-1}) + \frac{d\alpha_{lim}}{dM} (V - V^{k-1}) \quad (60)$$

where $\frac{d\alpha_{lim}}{dM}$ is computed by performing finite difference approximation as for the lift and drag coefficients discussed earlier.

Regarding environment-modelling assumptions, J_2 was used to meet the final landing-site requirements and to obtain optimal solutions, although it was not included when deriving the Jacobians for the gravitational acceleration. Similarly, it was found that the choice of atmospheric model had an effect on the entry corridor and could limit the vehicle manoeuvrability. Furthermore, the implications of assuming a spherical Earth on the guidance precision was also analysed, and it was decided to include the geodetic altitude and latitude to ensure that the vehicle did not miss the final landing site, although without inclusion in the Jacobian derivations.

The basic algorithm²² did not include the derivatives of the angle-of-attack profile with respect to speed (or Mach) in the state matrix. For the SPHYNX vehicle, this was seen to affect the algorithm convergence, because of the non-negligible Mach dependencies of the aerodynamics at transonic speeds and the non-convexities of the trimming boundaries imposed through Eq. (60) for variable angle-of-attack formulations.

For fixed angle-of-attack formulations, and applying the chain rule because of the dependency of the reference angle-of-attack profile with Mach, these derivatives are given as follows:

$$\frac{dC_D}{dM} = \frac{\partial C_D}{\partial M} + \frac{\partial C_D}{\partial \alpha} \frac{d\alpha}{dM} \quad \text{and} \quad \frac{dC_L}{dM} = \frac{\partial C_L}{\partial M} + \frac{\partial C_L}{\partial \alpha} \frac{d\alpha}{dM} \quad (61)$$

which were computed using spline interpolation and finite differences, and for the angle-of-attack profile, with finite differences using the same Mach spacing.

The initial conditions can be defined by the EIP for an orbital abort mode as follows:

$$R_0 = R_{EIP}, \lambda_0 = \lambda_{EIP}, \delta_0 = \delta_{EIP}, V_0 = V_{EIP}, \gamma_0 = \gamma_{EIP}, \chi_0 = \chi_{EIP} \quad (62)$$

while for a descent abort mode and reference trajectory update mode, these are defined by the current estimated states and controls:

$$\mathbf{x}_0 = \mathbf{x}_{est}, \mathbf{u}_0 = \mathbf{u}_{est} \quad (63)$$

although during implementation, the control variables \mathbf{u}_0 were allowed to vary by the limit imposed by the maximum rates.

The final DRS constraints, in terms of speed and altitude, compute an allowable box in the altitude-velocity plane. These are taken from **REQ-14**⁵¹ and are given as:

$$0 \text{ [m/s]} \leq V_f \leq a(h(t_f)) \quad \text{and} \quad 10 \text{ [km]} \leq h_f \leq 13 \text{ [km]} \quad (64)$$

It can be seen how the velocity represents a non-linear constraint because of its dependency with the final altitude, although it was assumed to belong to the troposphere and hence constant.

Another constraint from **REQ-14**⁵¹ is the minimum vertical velocity of -140 m/s. This is a non-linear function of the velocity and flight-path angle given as follows:

$$V_v(V_f, \gamma_f) = V_f \sin \gamma_f \geq -140 \text{ [m/s]} \quad (65)$$

while its linearised equivalent is the following function

$$V_v(V_f, \gamma_f) = V_v(V_f^{k-1}, \gamma_f^{k-1}) + V_{vV}(V_f^{k-1}, \gamma_f^{k-1})(V_f - V_f^{k-1}) + V_{v\gamma}(V_f^{k-1}, \gamma_f^{k-1})(\gamma_f - \gamma_f^{k-1}) \quad (66)$$

where V_{vV} , $V_{v\gamma}$ are the respective Jacobians given as follows:

$$V_{vV} = \frac{\partial V_v(V_f, \gamma_f)}{\partial V} = \sin \gamma_f \quad (67)$$

$$V_{v\gamma} = \frac{\partial V_v(V_f, \gamma_f)}{\partial \gamma} = V \cos \gamma_f \quad (68)$$

In addition to these, an additional constraint was introduced, which specifies that the DRS triggering should be within a 10 km radius from the designated landing site. This is imposed with a second-order cone constraint approximated with the average Earth radius as:

$$\|\lambda_{N-1} - \lambda_s, \delta_{N-1} - \delta_s\|_2 \leq \frac{10}{R_{avr}} [\text{km}] \quad (69)$$

This approximation does not compute the actual distance to the landing site, and a better approximation would be to approximate the range to go as a function of minimum and maximum longitude with a first-order or second-order Taylor series, as described in 51. Nevertheless, this condition guarantees that the final position is within a 10 km radius, with a maximum of around 8 km in the zonal direction.

Furthermore, bounds were introduced in the problem to avoid unrealistic scenarios and to allow for the automatic variable scaling routine. For the spherical coordinates, these are:

$$\begin{pmatrix} R_{avr} + 1000 \\ \lambda_{EIP} - 10^\circ \\ -52^\circ \\ 100 \\ -30^\circ \\ -10^\circ \end{pmatrix} \leq \begin{pmatrix} R \\ \lambda \\ \delta \\ V \\ \gamma \\ \chi \end{pmatrix} \leq \begin{pmatrix} R_{avr} + 126000 \\ \lambda_{EIP} + 270^\circ \\ 52^\circ \\ 1.05 \sqrt{\frac{\mu}{R_{avr}}} \\ 0.5^\circ \\ 270^\circ \end{pmatrix} \quad (70)$$

V. Analysis of Objective Functions and Formulations

A. Analysis of Objective Functions

A variety of objective functions can be considered for an optimum on-board planning guidance algorithm. For example, the integrated heat load $\int q_c dt$, a key re-entry guidance metric, can be minimised directly. Another suitable objective function can be to minimise the aerodynamic attitude rates $\int \sqrt{\dot{\alpha}^2 + \dot{\sigma}^2} dt$ which can prevent the characteristic control chattering seen in many non-linear programming optimisers. Time of flight t_f could also be selected as an objective function for different mission scenarios, especially during crew emergency missions requiring a rapid re-entry for to ensure safety. The maximum aerodynamic g-load, $\max n_g$, can also be minimised, especially during critical abort missions experiencing structural concerns. The same holds for the maximum heat flux, to reduce refurbishment efforts for reusable launchers. This can also be especially important for crewed missions during abort scenarios, where the crew could be facing life-threatening issues requiring minimum g-loads, and for commercial flights with inter-continental transportation vehicles as Starship of the Space Liner to reduce stress or fear of untrained crew, or simply to maximise passenger comfort.

The direct linearisation formulation with angle of attack rates was used to assess the suitability of the different objective functions. Table 2 provides some results showing the performance of the optimiser.

The results show that the extended successive convexification method could obtain optimal solutions for a variety of objective functions. Moreover, it was seen that the optimisation of both angle of attack and bank angle resulted in a coordinated control policy to meet all trajectory constraints while minimising an objective. The behaviour of the angle of attack history showed sometimes contradictory results with respect to the analyses performed in Sec. IV.A for the preliminary angle-of-attack design, especially during the final re-entry phases for the minimum final time and heat load as a result of the different constraints and large cross-range requirements.

Moreover, from a comparison between these objectives, it is possible to see that many of them involve conflicting trends. For example, the maximum heat flux minimisation resulted in large normal loads, while the minimum load resulted in a high heat flux densities. Similarly, reducing the heat flux resulted in considerably higher heat loads, as the trajectory continues for a longer time in the upper atmosphere region

Table 2. Results for the comparison between objectives for the nominal algorithm and environment settings and direct angle of attack and bank-angle formulation with algorithm performance metrics⁵¹

Objective	Objective Value	Final Time	Time Elapsed	SCOPT Iterations	Number of Warnings
Min Heat load	540.382 [MJ/m ²]	1711.45 [s]	85.0 [s]	23 [-]	2 [-]
Min Integrated Control Effort	56.05 [deg]	1650.00 [s]	34.3 [s]	13 [-]	0 [-]
Min Maximum Control Effort	0.058 [deg/s]	1734.78 [s]	52.9 [s]	22 [-]	0 [-]
Min Maximum Flight-path Rate	0.078 [deg/s]	1679.38 [s]	174.2 [s]	26 [-]	2 [-]
Min Maximum Heat Flux	561.96 [kW/m ²]	1710.95 [s]	147.7 [s]	24 [-]	5 [-]
Min Maximum g-load	1.111 [g's]	1696.38 [s]	65.4 [s]	20 [-]	0 [-]
Min Time of Flight	1525.05 [s]	1525.05 [s]	50.1 [s]	21 [-]	0 [-]
Min Site Miss Distance	4.7×10^{-8} [km]	1720.15 [s]	46.3 [s]	24 [-]	0 [-]

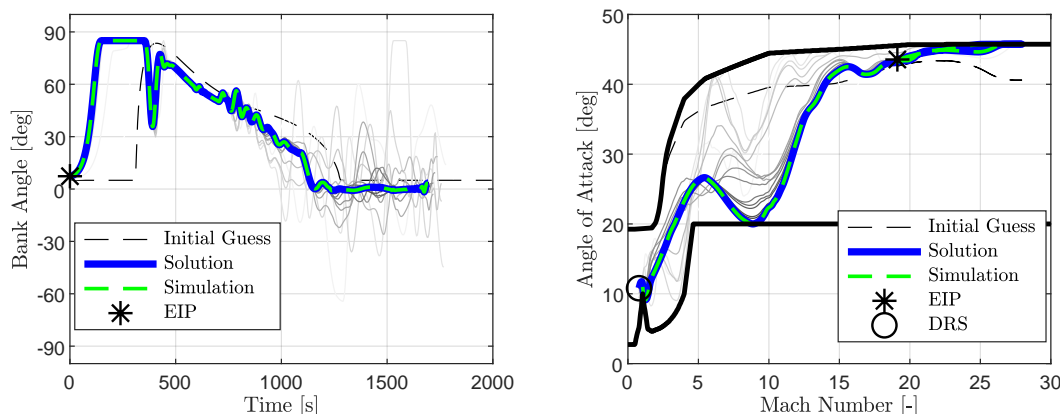


Figure 3. Aerodynamic attitude for the direct bank angle and angle of attack minimum maximum normal load (nominal environment and algorithm settings).

with lower drag, which at the same time required a larger loss of energy (drag) when flying at the lower atmospheric regions, explaining the high normal loads and excessive dynamic pressure.

Therefore, it was difficult to select a specific objective to design the integrated abort guidance. On one hand, the minimum site miss distance succeeds, satisfying all mission constraints within a small number of iterations, albeit by not minimising a characteristic performance metric. The minimum maximum normal load objective also resulted in promising results and was seen to be desirable for different aspects considering human-rated missions, although resulted in small final bank angles complicating tracking. The minimum maximum control effort not only resulted in the lowest integrated efforts, aero-thermal and mechanical loads, but achieved heat loads just 3% higher than the optimum and with the lowest computational effort, which increased its desirability as an abort guidance objective. On the other hand, the heat-load minimisation problem also provided adequate results for most formulations with smooth and feasible trajectories, while minimising a typical performance metric. It was therefore chosen to analyse the guidance planner in this research, although for actual mission implementation a more thorough analysis accounting for particular needs and trade-offs would be required.

B. Formulation Comparisons

In Secs. IV.B and IV.C, different formulations for the atmospheric re-entry problem with and without angle-of-attack optimisation were presented. Results for the maximum heat-load problem can be seen in Figs. 5

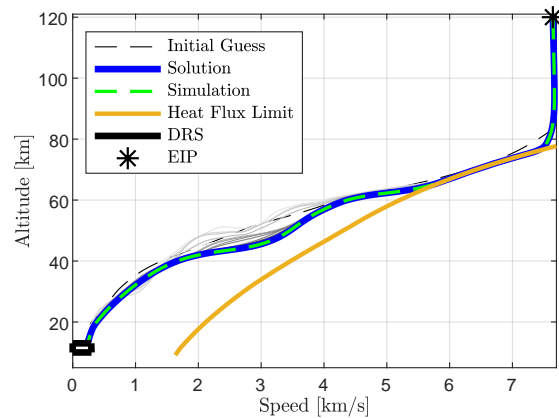


Figure 4. Geodetic altitude vs groundspeed for the direct bank angle and angle of attack minimum maximum normal load with nominal environment and algorithm settings

Table 3. Performance metrics for the different formulations in the minimum heat load optimisation.

Formulation	Heat Load	Final Time	Max g-load	Propagated Miss Distance	Average SOCP Iterations
Direct AOA and Bank	540.382 [MJ/m ²]	1711.45 [s]	1.922 [gs]	10.41 [km]	76 [-]
Hybrid	540.688 [MJ/m ²]	1722.70 [s]	1.754 [gs]	9.99 [km]	67 [-]
Direct Bank	573.476 [MJ/m ²]	1640.33 [s]	2.780 [gs]	9.96 [km]	48 [-]
Lossless Bank	573.455 [MJ/m ²]	1640.13 [s]	2.016 [gs]	60.51 [km]	54 [-]

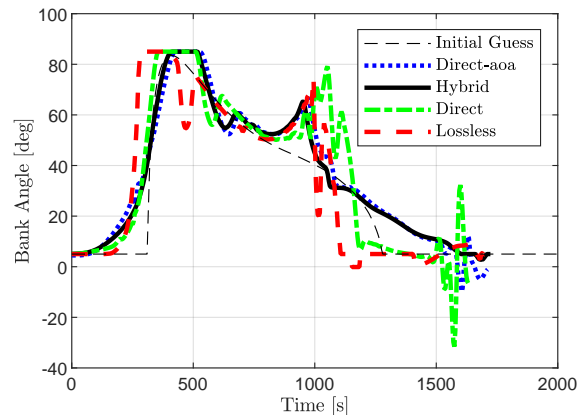


Figure 5. Bank-angle history for the minimum heat load optimisation problem with the extended successive convexification algorithm and different formulation.

and 6, and Table 3.

Figure 5 shows the bank-angle history during re-entry for the different formulations. It is seen how the direct linearisation approach of only bank angle suffered from large control chattering, which was only present during the final phase when angle of attack was included. In fact, a reduction of around 50% in the total integrated control effort was achieved, a figure which was also true for the other problems which converged with only bank-angle planning. This may be a consequence of convergence difficulties in the successive convexification algorithm, which benefits from added control degrees. A potential similar reason could be found for both approaches using the lossless convexification for bank angle, as it is replaced by two controls which are related with a relaxation condition. Moreover, it was seen that a lossless relaxation of the bank angle could satisfy the minimum absolute bank-angle limit of 5°, which could be beneficial for the

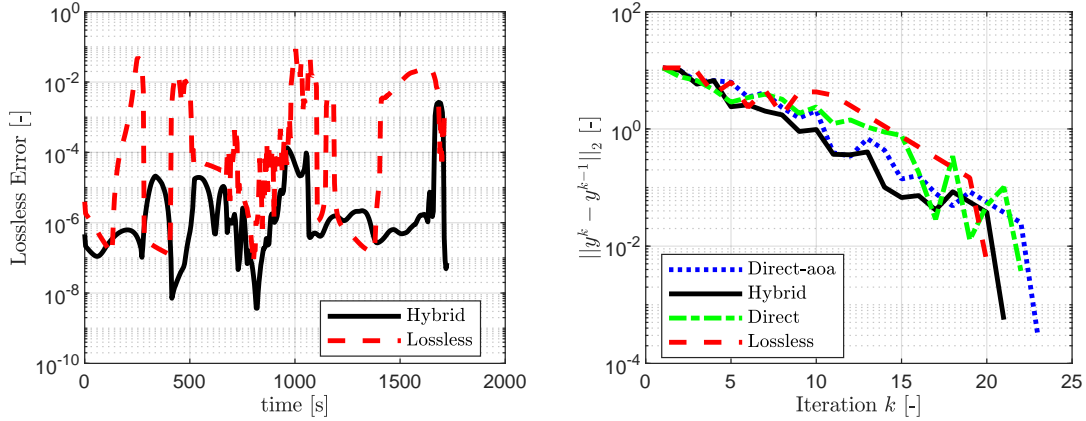


Figure 6. Lossless Error (left) and variables convergence (right) for the minimum heat load optimisation problem with the extended successive convexification algorithm and different formulations.

GNC system, since at low angles, bank-angle tracking becomes ineffective.

The relaxation from Eq. (39) was seen to be satisfied, see Fig. 6(a), for the most part of the re-entry, although some large peaks were present for the fix angle of attack case. This satisfaction was also less obvious for the hybrid approach. These two trends could be caused by a sub-optimal relaxation factor λ_χ , or because of a possible lack of relaxation proof.

It is also seen in Table 3 that when the angle of attack was included in the optimisation loop, the objective function was reduced by around 5.8%, which may not be a large value, but could result in relaxed TPS requirements. The time of flight was lower for the formulation not including time of flight as the angle of attack was closer to the top boundary at smaller Mach numbers, encountered when flying at lower parts of the atmosphere with higher dynamic pressures. This resulted in larger drag forces than for the formulation including angle of attack, and hence in a larger loss of specific energy and time of flight.

In addition, although it was not an objective, the aerodynamic load was minimised by an amount of almost 30%, which could be indicative of smoother trajectories. A smaller load reduction of around 9% was also seen for the minimum aerodynamic-load problem.

On average, including angle of attack directly in the optimisation increased optimality by 16% for those problems that converged. On the other hand, the number of successive iterations increased by 32% for all problems, with time elapsed almost doubling, because of the increased SOCP sub-problem iterations and the larger number of variables. Although this might be critical for on-board algorithms, dedicated software development for real-time applications in on-board hardware can significantly decrease this value.

Furthermore, the hybrid method was seen to converge slightly faster than the direct linearisation approach. Although it converged only two iterations before, the average number of iterations reduction for each SOCP sub-problem was around 7%. It also showed small negligible differences for the minimum heat flux and heat load optimum objectives, while converging on average in around 15% fewer iterations. Nevertheless, the hybrid approach failed to return flyable trajectories in most problems, highlighting the difficulty of properly selecting the regularisation term λ_χ .

On the other hand, the direct bank-angle optimisation was seen to converge in a smaller number of iterations than for the lossless convexification approach, although this could have been a consequence of a sub-optimal convergence or relaxation factors.

VI. Orbital and Descent Abort Analysis

A. Orbital Aborts

An orbital abort scenario with a landing site in Santa Maria in Azores was analysed by optimising the trajectory for minimum heat load and computing the EIP as in Ref. 51. A grid of possible entry longitudes and latitudes was computed with a 5° separation to assess the vehicle reachability capabilities, when using the successive convexification based trajectory planner described in Sec. IV.C. All computed trajectories that

Table 4. Results for the nominal algorithm and environment settings and direct angle of attack and bank-angle formulation (1/4)

	Heat Load	Final Time	Miss Distance	Max Heat Flux	Max g-load
Mean	564.859 [MJ/m ²]	1850.11 [s]	9.283 [km]	670.002 [kW/m ²]	2.271 [gs]
Standard Deviation	34.314 [MJ/m ²]	175.47 [s]	0.660 [km]	0.066 [kW/m ²]	0.480 [gs]
Maximum	630.185 [MJ/m ²]	2196.36 [s]	9.996 [km]	670.174 [kW/m ²]	3.000 [gs]
Minimum	490.266 [MJ/m ²]	1515.12 [s]	8.010 [km]	669.778 [kW/m ²]	1.330 [gs]

did not fail during successive iterations, were explicitly integrated as in Sec. V.A to assess their feasibility by checking for a miss-distance error lower than 40 km. It should be noted that the number of successful trajectories could be larger, as besides the virtual control terms, some artificial errors from the propagation may have been introduced. The results are shown in Figs. 7 to 12, with the nominal trajectory assessed in Sec. V, the optimum with worse heat load in red, and the optimum with best heat load in green.

Figure 7 shows the bank angle and angle of attack during re-entry. It is seen how trajectories bank mainly to the left or right, depending on their initial heading direction. Trajectories which start at longitudes which are further away perform re-entries requiring an anti-clockwise change in direction, and therefore negative banking to target the landing site, while the opposite holds for trajectories closer in longitude. It is also seen

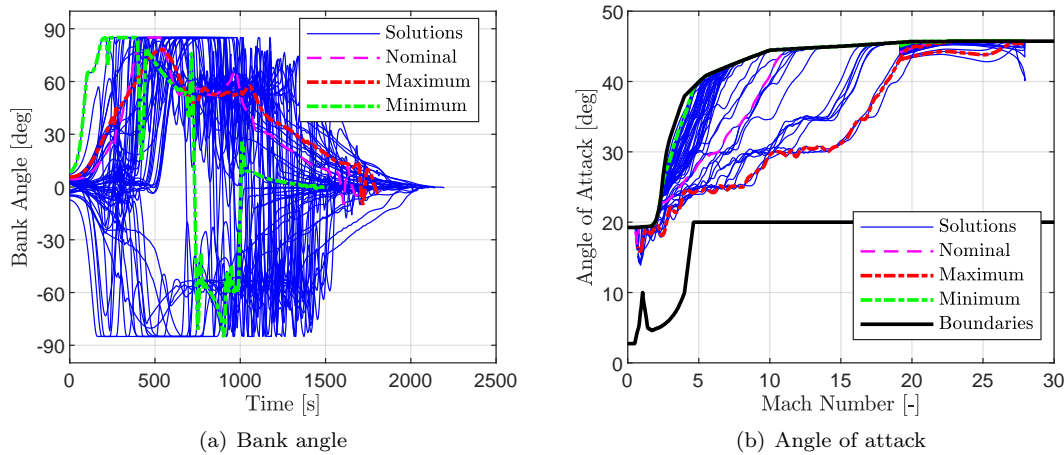


Figure 7. Aerodynamic attitude for the orbital abort EIP analysis for the minimum heat load optimisation problem with the extended successive convexification algorithm.

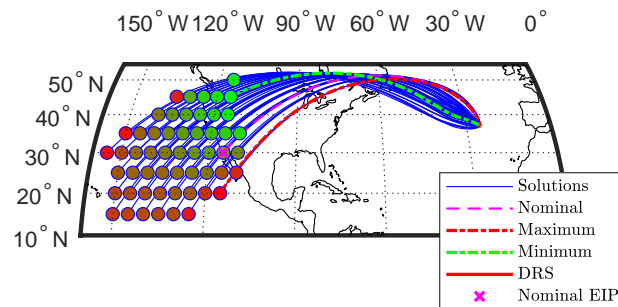


Figure 8. Geographic plot for the orbital abort EIP analysis for the minimum heat load optimisation problem with the extended successive convexification algorithm. The entry interfaces are coloured according to the achieved heat load, with green being the smallest and red being highest

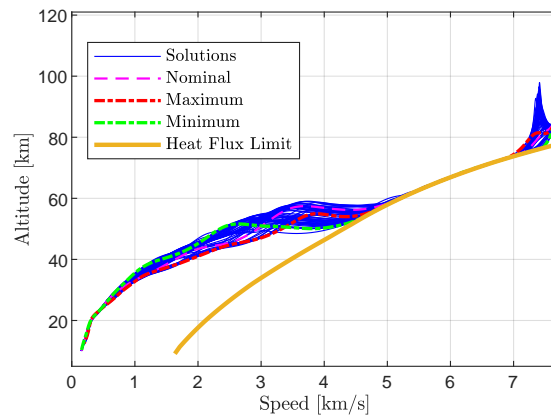


Figure 9. Altitude-speed plot for the orbital abort EIP analysis for the minimum heat load optimisation problem with the extended successive convexification algorithm.

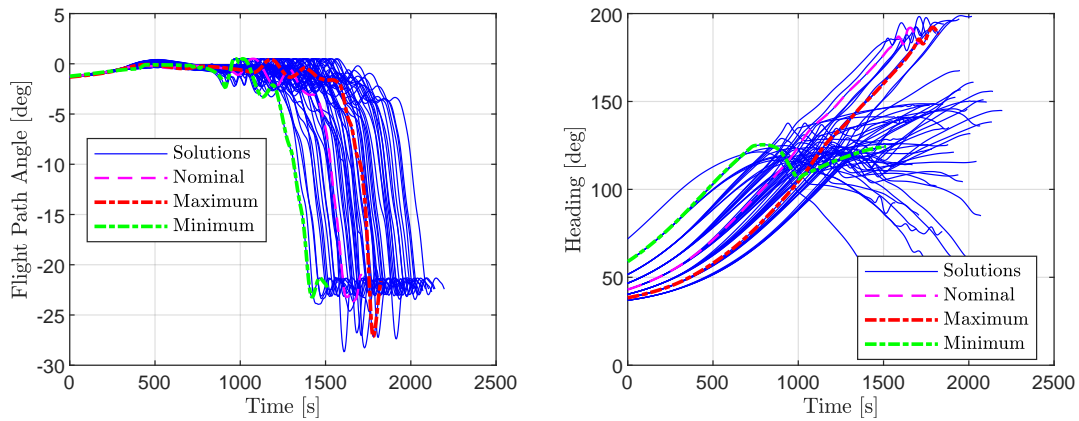


Figure 10. Flight-path angle (left) and heading angle (right) for the orbital abort EIP analysis for the minimum heat load optimisation problem with the extended successive convexification algorithm.

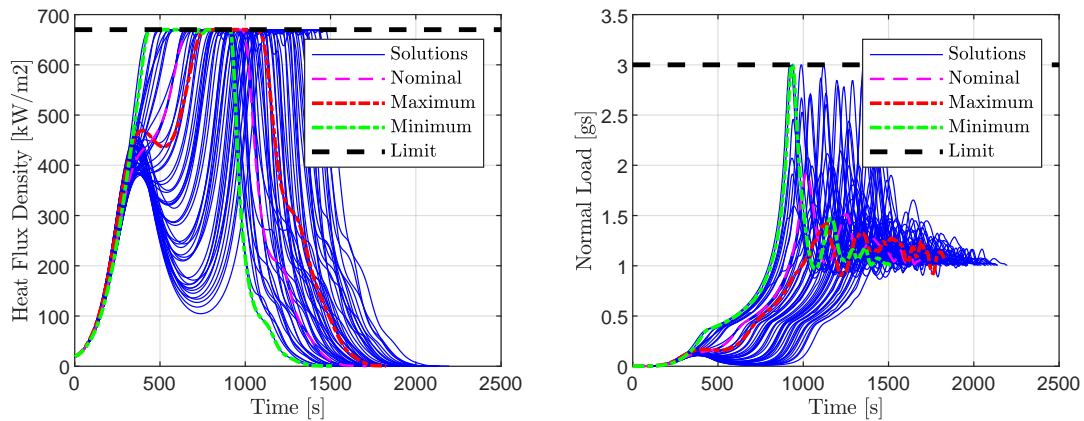


Figure 11. Heat flux (left) and normal load (right) for the orbital abort EIP analysis for the minimum heat load optimisation problem with the extended successive convexification algorithm.

how certain solutions require some bank reversals, as is the case for re-entry with lowest heat load. This is mostly seen in trajectories with low cross-range requirements, and the behaviour is similar to that one of the minimum time of flight optimisation, achieving high normal loads as seen in Fig. 11(b).

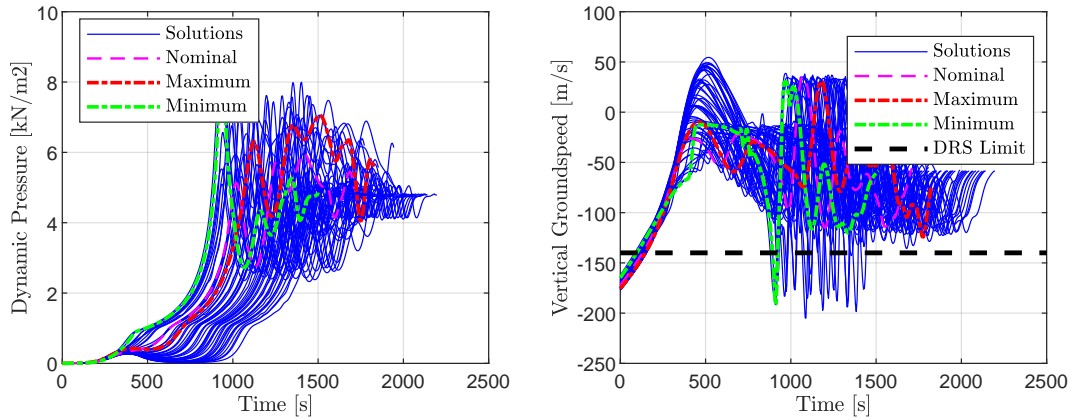


Figure 12. Dynamic pressure (left) and vertical groundspeed (right) for the orbital abort EIP analysis for the minimum heat load optimisation problem with the extended successive convexification algorithm. The limit for the vertical groundspeed is just imposed at the DRS interface.

Table 5. Results for the orbital abort reachability analysis with the nominal algorithm and environment settings and direct angle of attack and bank-angle formulation (2/4)

	DRS Altitude	DRS Mach Number	DRS Vertical Speed	Max Dynamic Pressure
Mean	10.37 [km]	0.533 [-]	-60.43 [m/s]	6.64 [kPa]
Standard Deviation	0.81 [km]	0.057 [-]	5.84 [m/s]	1.01 [kPa]
Maximum	12.73 [km]	0.712 [-]	-55.32 [m/s]	8.75 [kPa]
Minimum	10.01 [km]	0.507 [-]	-81.77 [m/s]	5.10 [kPa]

Table 6. Results for the orbital abort reachability analysis with the nominal algorithm and environment settings and direct angle of attack and bank-angle formulation showing algorithm performance metrics (3/4)

	$t_f \sum w_i \dot{\sigma} $	$\max \dot{\sigma} $	$t_f \sum w_i \dot{\alpha} $	$\max \dot{\alpha} $
Mean	566.1 [deg]	3.86 [deg/s]	41.2 [deg]	0.223 [deg/s]
Standard Deviation	235.8 [deg]	1.48 [deg/s]	6.1 [deg]	0.028 [deg/s]
Maximum	1030.1 [deg]	5.00 [deg/s]	59.2 [deg]	0.290 [deg/s]
Minimum	218.2 [deg]	0.91 [deg/s]	30.6 [deg]	0.170 [deg/s]

Table 7. Results for the orbital abort reachability analysis with the nominal algorithm and environment settings and direct angle of attack and bank-angle formulation with algorithm performance metrics (4/4)

	Time Elapsed	Iterations	Average SOCP Iterations	Warnings
Mean	75.5 [s]	21.8 [-]	72.88 [-]	1.5 [-]
Standard Deviation	26.57 [s]	3.5 [-]	22.11 [-]	3.3 [-]
Maximum	212.1 [s]	40.0 [-]	142.0 [-]	23 [-]
Minimum	28.9 [s]	14.0 [-]	41.24 [-]	0 [-]

In addition, a significant difference in the angle of attack versus Mach number plot is seen between the trajectories with highest and lowest heat load. The former ones are seen to fly at lower angles of attack, as they are faced with higher range requirements, resulting in larger flight times and heat loads. Contrary, the latter ones can use higher angles of attack near the maximum trimming boundary to increase drag and reduce the time of flight, and hence the integrated heat load.

This effect of the range and cross-range requirements on the minimum heat load can also be seen in Fig. 8, where the coloured EIP represents the achieved optimal heat load for the entry interface point. The figure shows how trajectories with higher initial range and cross-range requirements suffer from high heat loads during re-entry, as the optimal law is more constrained. This is also seen in the bank angle profile from Fig. 7(a), where the nominal re-entry has a lower bank angle than the maximum heat load re-entry, as it requires

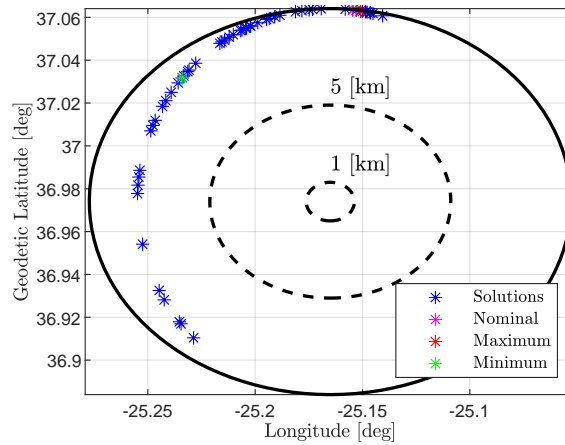


Figure 13. Miss distance for orbital abort EIP analysis for the minimum heat load optimisation problem with the extended successive convexification algorithm. The entry interfaces are coloured according to the achieved heat load, with green being the smallest and red being highest

excessive anti-clockwise banking to meet the initial cross-range requirement. It has to be noted that the reachability map shows a considerably lower coverage than that identified in Ref. 25. This may be caused by the definition of feasible trajectories, which was dependent on the number of nodes used, and because the flight-path angle was constrained to a maximum of 0.5° to avoid skipping flight. Furthermore, it was not known whether the ASTOS optimiser used an adaptive mesh-refinement procedure nor its collocation strategy.

Furthermore, the altitude versus velocity plot in Fig. 9 and the heat-flux history in Fig. 11 show all trajectories initially flying near the maximum heat flux boundary to maximise drag and reduce the integrated time flying over areas resulting in high heat flux. In addition, although the trajectory was constrained with a maximum flight-path angle of 0.5° , the former figure also shows an initial skip for the largest heat load trajectory, which is a consequence of the large range requirement for certain trajectories. This can also be noticed in the flight-path angle history in Fig. 10.

Figures 11 and 12 show that all trajectories are able to meet the maximum heat-flux and normal-load path constraints, while satisfying the lower boundary in the minimum vertical speed for DRS triggering. In addition, the dynamic pressure, although not constrained, was shown to remain low, even for the minimum achievable heat load case, contrary to what was seen for the minimum time of flight optimisation. Finally, Fig. 13 confirms that all optimum trajectories can successfully meet the final miss-distance constraint.

It is also seen in Fig. 7 that the amount of time elapsed to compute the optimum solutions was in the order of 1 minute with significant variability. This is not desired for on-board applications, but because of the current non-optimised software and the indications regarding the suitability for real-time applications, it is assumed that the real-time computation could be smaller. Some warnings associated to numerical issues were also present. Although the trajectories were discarded, it would be necessary to address this issue in future studies before moving on to real-time applications.

B. Descent Aborts

In addition to orbital aborts, descent abort may occur during re-entry as a consequence of landing-site unavailability, because of external causes. If a vehicle has already performed a de-orbit burn, it might not have enough propellant to steer towards a different EIP to land on an alternative landing site. The nominal site in Santa Maria in Azores shared the same EIP as other landing sites in Canary Islands and in Ben Guerir Air Force Base. This section shows results for aborts towards the latter case.

During the optimisation campaign, it was difficult to obtain optimum trajectories when the final miss distance was considered as a hard constraint, especially for early aborts. This artificial infeasibility was thought to be a consequence of the hard thrust-region radius and the virtual controls choice, and could be solved by re-tuning the optimisation parameters or including a virtual buffer. Nevertheless, because of research time constraints, it was preferred to switch to a minimum miss-distance problem for the aborted trajectory. This can also be a safe choice for an on-board abort, as after an abort has been performed, the prime requirement should be to reach the alternative site safely.

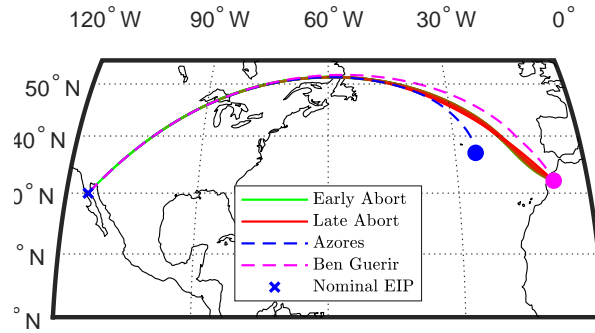


Figure 14. Geographic plot showing the descent aborts for the minimum heat load optimisation problem with the extended successive convexification algorithm.

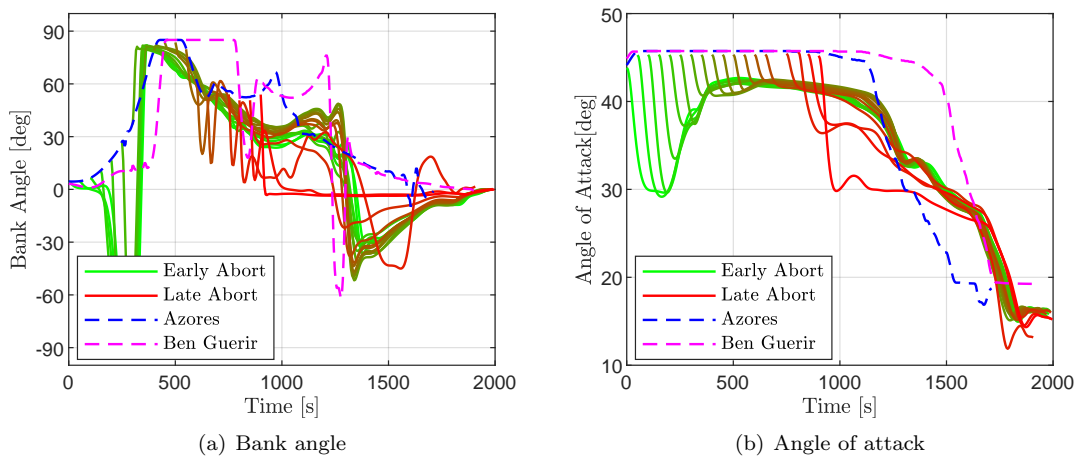


Figure 15. Aerodynamic attitude for the descent abort analysis for the minimum heat load optimisation problem with the extended successive convexification algorithm.

The methodology to analyse these capabilities was to explicitly integrate the orbital re-entry, while time-tracking the pre-planned abort trajectory. The descent abort was then triggered at different time steps with intervals of 50 s, and the resulting trajectories were stored and loaded on-board as the new references.

As for the orbital abort study, a trajectory was considered feasible when it resulted in optimal solutions satisfying the final miss distance requirement of a 10-km maximum, and which had propagated solutions with a miss distance lower than 40 km from the alternative landing site. Furthermore, intervals of 50 s for the descent abort time t_A were considered.

Figure 14 shows the abort trajectories in terms of longitude and geodetic latitude. Feasible results were obtained up to $t_A \leq 900$ s, as shown in Figs. 14 to 16, although the abort performed at $t_A = 700$ s was seen to fail (this could be corrected with different heuristic values).

In addition, Fig. 15 shows the bank-angle and angle-of-attack histories. From these, one can see how the descent guidance performs the abort, changing the remaining of the aerodynamic attitude histories and the resulting altitude and velocity trajectories (Fig. 16).

It should be noted that only around 900 seconds are available to perform an abort while re-entering, which could put strict requirements on the on-board computation of the planner trajectory. Therefore, flight hardware used for abort missions based on optimum planner would need to have large computational capabilities, or other landing areas should be considered.

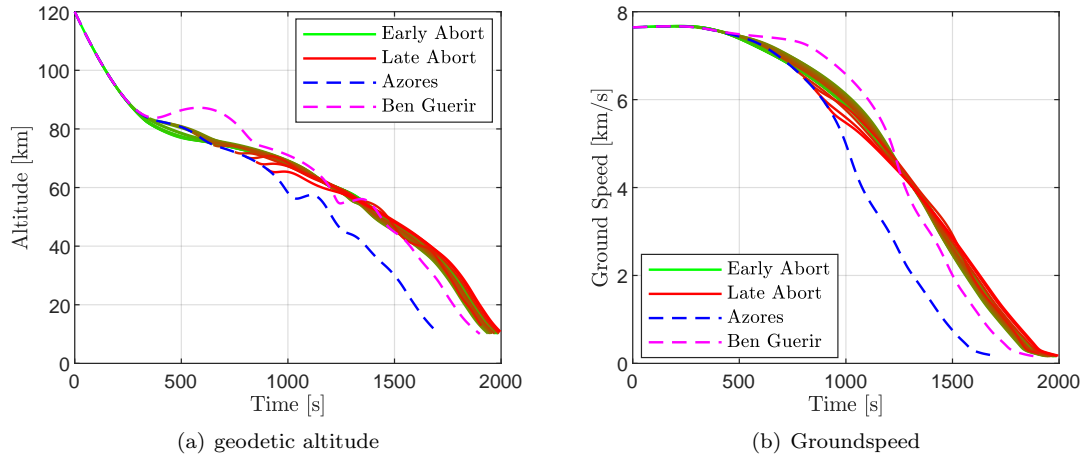


Figure 16. Descent aborts for the minimum heat load optimisation problem with the extended successive convexification algorithm.

VII. Conclusions and Recommendations

The study shows that it is possible to develop a generalised successive convex optimisation framework for aerospace optimal-control problems. This can contribute to a high automation of mission planning and GNC, and can be used to obtain realistic optimum trajectories for atmospheric re-entry. But, only as long as adequate strategies to account for non-convexities as incorporating virtual controls, virtual buffers, adaptive thrust regions and line-search are used. The minimum control-effort and miss-distance problem were seen to have the best numerical convergence properties, and the algorithm showed faster convergence when removing virtual controls and buffers. This could be done for on-board updates using the trajectory optimised at the previous guidance cycle. The extension of angle-of-attack planning led to higher optimality and feasibility, albeit with an increase in computational time.

It was seen that, although lossless bank-angle relaxation increased convergence, while obtaining negligible differences in the objective function, it required significant trial and error for its augmentation weight (λ_χ) to provide flyable trajectories respecting the relaxation condition, thus decreasing its adaptiveness.

The successive convexification strategy was also extended to include a golden-section search method and combined with virtual controls, virtual buffers, an adaptive thrust region to increase the robustness against non-convexities. The largest source of convergence issues was seen to be the tabulated aerodynamic database, which was evaluated on-line with multi-variate interpolation of angle of attack and Mach number and used a finite difference approximation to evaluate its derivatives. This introduced large discontinuities during the successive evaluations, as expected for a local optimisation method. Using the derivative-free golden-section search allowed to obtain solutions in many problems, which did not converge before, and to reduce the number of iterations by almost 20%. Furthermore, augmenting the heat flux constraint with a virtual buffer into the objective function provided larger robustness to the initial guess.

All in all, it is concluded that there is a large margin of improvement, which could enhance its feasibility and robustness, and that the software implementation on flight-ready hardware could increase its capabilities for real-time on-board applications.

Regarding potential improvements, future work could analyse pseudo-spectral, advanced collocation methods, and off-line mesh-refinement strategies. This can reduce the number of nodes and increase the solution accuracy. Similarly, the problem heuristics as the thrust regions and virtual control terms can also be optimised off-line or changed adaptively during the on-board implementation, and the suitability of different line search algorithms can be assessed. Additionally, specific SOCP solvers for sequential solutions and embedded applications can also be designed, and a performance comparison with different commercial non-linear programming solvers can be performed.

In addition to this highly optimum planner, future studies could be focused on assessing the necessary adaptations for on-board updates with or without virtual controls and buffer zones, and on exploring a trade-off between high optimality during on-board planner updates and tracking guidance performance

with a Monte Carlo campaign. This removed fidelity could also facilitate the removal of non-convexities and increase the computational performance. For example, adequate approximations to the aerodynamic database could be derived, as it was seen that the polar approximation could reduce computational time by 40%, although in the current application it could not capture the hypersonic aerodynamic behaviour. The energy domain could also be compared, together with the effects of decoupling the longitudinal and lateral motion. Angle of attack planning can also be left to an outer loop to plan for the η_α on-board, or directly inserting it as an optimisation parameter.

Regarding the orbital and descent abort guidance design and reachability capabilities, the performance of different objective functions and the fully implemented closed-loop guidance could be assessed, and additional landing sites and EIPs can be considered to better characterise the abort capabilities off-line. The inclusion of no-fly zones over restricted or populated areas can be incorporated to assess the implications on reachability capabilities. Finally, a landing-site selection logic can also be designed based on different metrics obtained from the on-board planner.

References

- ¹Graves, C.A. and Harpold, J.C., “Apollo Experience Report: Mission Planning for Apollo Entry”, NASA-TN-D-6725, NASA, 1972.
- ²Bryson A.E., Carroll, E.J., Zvara, J., Black, A., Blatt, P., Bohling, R., Burke, M., Kanter, J. Lickly, D., Morth, R., Rosamond, D. and Wingrove, R., “Guidance and navigation for entry vehicles”, NASA-SP-8015, NASA, 1968.
- ³Mease, K.D., Chen, D.T., Teufel, P. and Schonenberger, H., “Reduced-order entry trajectory planning for acceleration guidance”, *Journal of Guidance, Control and Dynamics*, 25(2):257-266, 2002. doi: 10.2514/2.4906
- ⁴Harpold, J.C. and Graves, C.A., “Shuttle Entry Guidance”, *Journal of the Astronautical Sciences*, XXVII(3):239-268, 1979.
- ⁵Roenneke, A.J. and Markl, A., “Re-entry control to a drag-vs-energy profile”, *Journal of Guidance, Control and Dynamics*, 17(5):916-920, 1994. doi: 10.2514/3.21290
- ⁶Lu, P., “Entry Guidance and Trajectory Control for Reusable Launch Vehicle” *Journal of Guidance, Control and Dynamics*, 20(1):142-149, 1997. doi: 10.2514/2.4008
- ⁷Grimm, W. van de Meulen, J.G. and Roenneke, A.J., “Update scheme for drag reference profiles in an entry guidance”, *Journal of Guidance, Control and Dynamics*, 26(5):695-701, 2003. doi: 10.2514/2.5123
- ⁸Zimmerman, C., Dukeman, G. and Ganson, J., “Automated method to compute orbital reentry trajectories with heating constraints”, *Journal of Guidance, Control and Dynamics*, 26(4):523-529, 2003. doi: 10.2514/2.5096
- ⁹Saraf, A., Leavitt, J.A., Chen, D.T. and Mease, K.D. “Design and Evaluation of an acceleration guidance algorithm for entry”, *Journal of Spacecraft and Rockets*, 41(6):986-996, 2004. doi: 10.2514/1.11015
- ¹⁰Leavitt, J.A. and Mease, K.D., “Feasible trajectory generation for atmospheric entry guidance” *Journal of Guidance, Control and Dynamics*, 20(2):473-481, 2007. doi: 10.2514/1.23034
- ¹¹Shen, Z. and Lu, P., “On-board generation of three-dimensional constrained entry trajectories”, AIAA Guidance, Navigation and Control Conference and Exhibit, American Institute of Aeronautics and Astronautics, 2002.
- ¹²Betts, J.T. “Survey of numerical methods for trajectory optimization”, *Journal of Guidance, Control and Dynamics*, 21(2):193-207. 1998. doi: 10.2514/2.4231
- ¹³D’Souza, S.N. and Sarigul-Klijn, N., “Survey of planetary entry guidance algorithms”, *Progress in Aerospace Sciences*, 68:64-74, 2014. doi: 10.1016/j.paerosci.2014.01.002
- ¹⁴Sagliano, M., “Generalized hp pseudospectral convex programming for powered descent and landing”, *Journal of Guidance, Control and Dynamics*, 41(2):320-334, 2018. doi: 10.2514/1.G002818
- ¹⁵Wang, Z. and Grant, M.J., “Hypersonic Trajectory Optimization by Sequential Semidefinite Programming”, AIAA Atmospheric Flight Mechanics Conference, 2017. doi: 10.2514/6.2017-0248
- ¹⁶Shen, Z. and Lu, P., “Dynamic lateral entry guidance logic”, *Journal of Guidance, Control and Dynamics*, 27(6):949-959, 2004. doi: 10.2514/1.8008
- ¹⁷Bharadwaj, D., Rao, A.V. and Mease, K.D., “Entry trajectory tracking law via feedback linearization”, *Journal of Guidance, Control and Dynamics*, 21(5):726-732, 1998. doi: 10.2514/2.4318
- ¹⁸Lu, P., “Regulation about time-varying trajectories: precision entry guidance illustrated”, *Journal of Guidance, Control and Dynamics*, 22(6):784-790, 1999. doi: 10.2514/2.4479
- ¹⁹Sagliano, M., Samaan, M., Theil, S. and Mooij, E. “SHEFEX-3 optimal feedback entry guidance”, AIAA Space Conference and Exposition, 2014.
- ²⁰Sagliano, M. and Mooij, E., “Optimal Drag-Energy Entry Guidance via Pseudospectral Convex Optimization”, AIAA Guidance, Navigation and Control Conference, 2018.
- ²¹Acikmese, B. and Ploen, S.R., “Convex Programming approach to powered descent guidance for mars landing”, *Journal of Guidance, Control and Dynamics*, 2007. 30(5):1353-1366, doi 10.2514/1.27553.
- ²²Wang, Z. and Grant, M.J., “Constrained trajectory optimization for planetary entry via sequential convex programming”, *Journal of Guidance, Control and Dynamics*, 40(10):2603-2615, 2017. doi: 10.2514/1.G002150
- ²³Liu, X. and Shen, Z. and Lu, P., “Entry trajectory optimization by second-order cone programming”, *Journal of Guidance, Control and Dynamics*, 39(2):227-241, 2016. doi: 10.2514/1.G0011210
- ²⁴Sagliano, M. “Development of a Novel Algorithm for High Performance Reentry Guidance”, PhD thesis, 2016.

- ²⁵Gonzalez Puerta, A., Mooij, E. and Yabar Vallesz, C., “Reachability Analysis to Design Zero-Wait Entry Guidance, AIAA-2018-1316, *AIAA SciTech Forum*, Kissimmee, Florida, 8-12 January, 2018.
- ²⁶Lu, P. “Entry Guidance: A Unified Method”, *Journal of Guidance, Control and Dynamics*, 37(3):713–728, 2014. doi: 10.2514/1.62605.
- ²⁷Schierman, J.D., Ward, D.G., Hull, J.R., Gandhi, N., Oppenheimer, M.W. and Doman, D.R., “Integrated Adaptive Guidance and Control for Re-entry Vehicles with Flight-test results”, *Journal of Guidance, Control and Dynamics*, 27(6):975–988, 2004, doi: 10.2514/1.10344.
- ²⁸Betts, J.T. *Practical Methods for Optimal Control and Estimation using Non-linear programming*, 2ed. SIAM, 2010.
- ²⁹AIAA, “Special Issue on Computational Guidance and Control”, *Journal of Guidance, Control and Dynamics*, 40(2), 2017.
- ³⁰Simplicio, P., Marcos, A. and Bennani, S., “Guidance of Reusable Launchers: Improving Descent and Landing Performance”, *Journal of Guidance, Control and Dynamics*, 42(10):2206-2219, 2019. doi: 10.2514/1.g004155
- ³¹Rao, A. and Clarke, K., “Performance Optimization of a Maneuvering Re-Entry Vehicle Using a Legendre Pseudospectral Method”, AIAA Atmospheric Flight Mechanics Conference and Exhibit, American Institute of Aeronautics and Astronautics, 2002.
- ³²Jorris, T.R. “Common aero vehicle autonomous re-entry trajectory optimization satisfying waypoint and no-fly zone constraints”, PhD thesis, 2007.
- ³³Bollino, K., Ross, M. and Doman, D., “Optimal nonlinear feedback guidance for re-entry vehicles”, AIAA Guidance, Navigation and Control Conference and Exhibit, American Institute of Aeronautics and Astronautics, 2006.
- ³⁴Han, P., Shan, J. and Meng, X., “Re-entry trajectory optimization using an hp-adaptive radau pseudospectral method”. Proceedings of the Institution of Mechanical Engineering, Part G: Journal of Aerospace Engineering, 227(10):1623-1636, 2012. doi: 10.1177/0954410012461745
- ³⁵Blackmore, L., “Autonomous Precision Landing of Space Rockets”, *The Bridge: Linking Engineering and Society*, 46(4) National Academy of Engineering
- ³⁶Scharf, D.P., Acikmese, B., Dueri, D., Benito, J., Casoliva, J., “Implementation and Experimental Demonstration of Onboard Powered-Descent Guidance”, *Journal of Guidance, Control and Dynamics*, 40(2):213-229, doi: 10.514/1.G000399.
- ³⁷Boyd, S. and Vandenberghe, L., *Convex Optimization*, 7 ed. Cambridge University Press, 2009.
- ³⁸Hazra, S. “Autonomous Guidance for Asteroid Descent using Successive Convex Optimization”, MSc thesis Delft University of Technology and DLR, 2019.
- ³⁹Liu, X. and Lu, P. “Solving Nonconvex Optimal Control problems by convex optimization”, *Journal of Guidance, Control and Dynamics*, 37(3):750-765, doi: 10.2514/1.62110
- ⁴⁰Mao, Y., Szmuk, M., and Acikmese, B. “Successive convexification of non-convex optimal control problems and its convergence properties”, IEEE 55th Conference on Decision and Control (CDC), IEEE, 2016.
- ⁴¹Mao, Y., Szmuk, M., Xu, X. and Acikmese, B., “Successive convexification: a superlinearly convergent algorithm for non-convex optimal control problems”, *SIAM Journal on Control and Optimization*, 2018.
- ⁴²Wang, J. and Cui, N., “A Pseudospectral-Convex Optimization Algorithm for Rocket Landing Guidance”, AIAA Guidance, Navigation and Control Conference, American Institute of Aeronautics and Astronautics, 2018.
- ⁴³Szmuk, M. and Acikmese, B. “Successive Convexification for a 6-DoF Mars Rocket Powered Landing with Free-final time”, AIAA Guidance, Navigation and Control Conference, American Institute of Aeronautics and Astronautics, 2018.
- ⁴⁴Liu, X. “Fuel-Optimal Rocket Landing with Aerodynamic Controls”, AIAA Guidance, Navigation and Control (GNC) Conference, 2017. doi: 10.2514/6.2017-1732
- ⁴⁵Wang, Z. and Grant, M.J., “Autonomous Entry Guidance for Hypersonic Vehicles by Convex Optimization”, *Journal of Spacecraft and Rockets*, 55(4):993-1006, 2018. doi: 10.2514/1.A34102.
- ⁴⁶Wang, Z., “Maximum-Normal-Load Entry Trajectory Optimization for Hypersonic Glide Vehicles”, AIAA Scitech Forum, 2019.
- ⁴⁷Wang, Z. and Grant, M.J., “Improved Sequential Convex Programming Algorithms for Entry Trajectory Optimization”, AIAA Scitech Forum, 2019.
- ⁴⁸Zhao, D.J. and Song, Z.Y., “Reentry trajectory optimization with waypoint and no-fly zone constraints using multiphase convex programming”, *Acta Astronautica*, 137:60-69, 2017. doi: 10.1016/j.actaastro.2017.04.013
- ⁴⁹Yu, C.M., Zhao, D.Z. and Yang, Y., “Efficient Convex Optimization of Reentry Trajectory via the Chebyshev Pseudospectral Method”, *International Journal of Aerospace Engineering*, 2019. doi: 10.1155/2019/1414279.
- ⁵⁰Mooij, E., *The motion of a vehicle in a planetary atmosphere*, Delft University Press, 1997.
- ⁵¹Dominguez Calabuig, G.J., “Optimum On-board Abort Guidance based on Successive Convexification for Atmospheric Re-Entry Vehicles”, MSc thesis, Delft University of Technology, 2020.
- ⁵²Saraf, A., Leavitt, J.A., and Mease, K.D., “Landing Footprint Computation for Entry Vehicles”, 6-19 August, 2004. doi: 10.2514/6.2004-4774
- ⁵³Chen, T.Y., “Calculation of the move limits for the sequential linear programming method”, *International Journal for Numerical Methods in Engineering*, 36(5):2661-2679, 1993. doi: 10.1002/nme.1620361510.
- ⁵⁴Sobieszczanski-Sobieski, J., Morris, A., van Tooren, M., La Rocca, G. and Yao, W., “Multidisciplinary Design Optimization Supported by Knowledge Based Engineering”, 1ed, 2015, United Kingdom: John Wiley & Sons, Ltd.
- ⁵⁵Yang, R. and Liu, X., “Comparison of Convex optimization-based approaches to solve non-convex optimal control problems”, AIAA Scitech Forum, 2019.
- ⁵⁶Benedikter, B., Alessandro, Z. and Guido, C., “A convex approach to rocket ascent trajectory optimisation”, EUCASS 2019, Madrid, July, 2019.